(NASA-CR-143927) STUDY OF THE PERFORMANCE OF ANTENNAS IN MAGNETIZED PLASMAS Final Report (TRW Systems Group) 46 p HC $3.75 CSCL 17B

N75-30390

Unclas
G3/32 34310

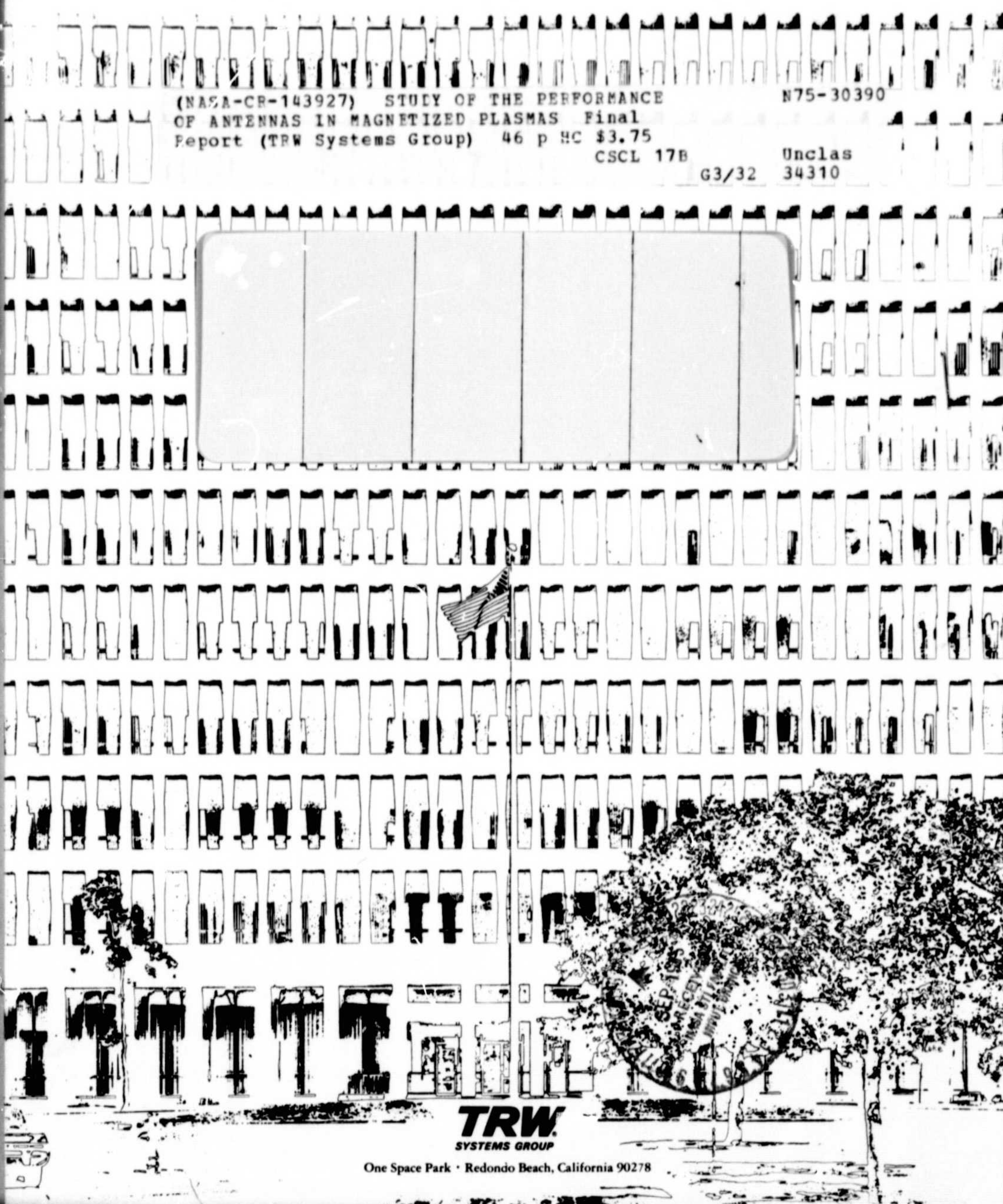

TRW SYSTEMS GROUP
One Space Park · Redondo Beach, California 90278

STUDY OF THE PERFORMANCE OF ANTENNAS IN MAGNETIZED PLASMAS

Final Report

#27468-6004-RU-00 June 30, 1975

NAS8-31175

Prepared for:

George C. Marshall Space Flight Center
Huntsville, Alabama 35812

Project Manager: R.W. Fredricks,
Member, Professional Staff

Principal Investigator: R.L. Stenzel
Member, Professional Staff

TRW Systems Group Research Staff
One Space Park,
Mail Station: R1/1070
Redondo Beach, CA 90278
Telephone: (213) 536-1105

Plasma Physics Group
Systems Group Research Staff

TRW SYSTEMS GROUP
One Space Park
Redondo Beach, CA 90278

I. EXPERIMENTAL SET-UP

The antenna studies are performed in the TRW Large Magnetized Plasma Source[1] (LAMPS), a schematic drawing of which is shown in Figure 1. A plasma column of diameter $d \approx 40$ cm and length $L \approx 300$ cm is produced by a dc discharge with a large (45 cm dia.), indirectly heated, oxide-coated cathode and adjacent mesh anode. The plasma is confined by a uniform axial magnetic field ($0<B_o<150$ gauss, temporal $\delta B/B_o<10^{-4}$, spatial $\delta B/B \approx \pm 0.5\%$) produced by a set of 8 external solenoidal coils driven with a transistor-regulated power supply (15V, 2000A). Axial plasma confinement is achieved with a multimirror permanent magnet wall[2] consisting of 200 samarium cobalt magnets ($B_{max} \approx 4$ kG) mounted in arrays of opposite polarity. Due to the magnetic confinement and the relatively efficient plasma production a large volume (450 liter), high density ($n_e \approx 10^{12} cm^{-3}$), collisionless ($\nu_{en}/\omega \approx 10^{-3}$, krypton $p < 5 \times 10^{-4}$ Torr, $kT_e \approx 2$ eV) plasma is produced at moderate input powers (discharge power 40Vx250A=10kW, heater power 25Vx360A=9kW). Density and magnetic field are independently variable, the electron temperature varies from $kT_e \approx 2$ eV$\approx 10\ kT_i$ during the discharge to $kT_e \approx .2$ eV$\approx kT_i$ in the late afterglow of a pulsed discharge, and various rare gases or mixtures with mass 4 (helium) to 131 (xenon) can be chosen. By pulsing the discharge which reduces the thermal load on cathode, probes and structures one has a choice of different electron distribution functions: during the discharge a tail of energetic electrons are present, in the afterglow the plasma is essentially Maxwellian in a uniform magnetic field but may develop a loss-cone distribution in a mirror-field configuration.

The plasma diagnostics consist of a 70 GHz (4 mm) microwave interferometer for density measurements and of various Langmuir probes for spatially resolved measurements of T_e, n_e and the shape of the electron distribution function. All diagnostic data are time-resolved by sample-and-hold techniques so as to yield information about the plasma build-up, the steady-state discharge and the plasma decay in the afterglow.

Whistler waves are excited and detected with various antennas which are inserted into the center of the plasma column through one axial and two orthogonal radial ports. The horizontal radial port and the axial port are equipped with a gate valve and decompression chamber so that probes can be exchanged while the machine is under operation. There are linear motorized probe drive systems installed on the radial and axial ports while the vertical probe has a circular motor drive which rotates the probe by 360° around the vertical axis. The tip of the vertical probe thus describes a circle whose radius ρ is varied by inclining the bellow-mounted probe shaft with respect to the vertical and whose plane of rotation is adjusted by moving the probe shaft through a sliding seal. The antennas used so far are shown in Figure 2. A balun-fed electric dipole (L_d=5 cm) dipole is mounted on the axial probe. Although the dipole balancing with a $\lambda/2$-line is frequency-dependent it eliminates the need for a second long, lossy and expensive high temperature coaxial cable. The electric dipole on the vertical probe is frequency-independent since it is balanced externally with a broadband hybrid tee. A similar electric dipole is also installed on the radial port. The magnetic loop on the radial probe shaft consists of a single-turn electrostatically shielded loop. The break in the shield is on the symmetry axis so that the electrostatic pick-up on the outer shield cancels. A similar magnetic loop is installed on the vertical probe shaft. Finally, a short wire (1 cm exposed center conductor) coaxial rf probe is installed from a top port near the cathode. This probe can be moved radially (vertically and horizontally on an arc) and is used for long distance wave propagation through the full length of the machine ($L>100\lambda_{||}$).

The antennas are tested for their proper dipole response and then calibrated in a known field geometry in air. For the electric dipole a parallel-plate capacitor field is used; the magnetic loop is calibrated in the near-zone field of a long linear conductor of known rf current distribution (matched $\lambda/2$ dipole).

The response of the magnetic loop is not affected by the presence of the plasma (μ=1) so that absolute wave magnetic field measurements are possible. The electric dipole response is substantially altered by the anisotropic susceptibility of the plasma; no attempts for measuring the absolute wave electric field are done so far.

2. ANTENNA RADIATION PATTERN

Antenna radiation patterns are measured with the setup shown in Figure 3. The rf signal (pulsed or steady-state, $50<f<200$ MHz, $P_{rf}\leq 150$W) is applied to the exciter antenna and received with a second antenna which can move on a circle ($0<\rho<25$ cm, $-90°<\phi<+90°$) around the exciter. The rf amplitude is obtained from a spectrum analyzer tuned manually to the incident frequency. The spectrum analyzer output is sampled at a desired time during the discharge or afterglow, averaged over many discharge pulses (500 msec repetition time) and plotted versus angle ϕ.

Due to the variety of parameters the results will be grouped by type of antenna, density regime and applied rf power level.

2.1 Electric Dipole

2.1.1 Density Dependence

Figure 4 shows the antenna radiation pattern of the axial electric dipole as detected with the vertical dipole at different densities in the small amplitude regime. At low densities [$n_e < 10^{10}\text{cm}^{-3}$, $\omega_p/\omega = 0(1)$] where both the dipole length (5 cm) and the antenna separation ($\sim$ 10 cm) are small compared to the characteristic whistler wavelength ($\lambda_{||} \approx 100$ cm) the antenna exhibits the well-known resonance cone patterns.[3,4] No interference structure due to warm plasma modes is observed which may be explained by the still relatively large size of the exciter in terms of warm plasma mode wavelengths ($L_{\text{dipole}} >> v_{th}/\omega_p$).

With increasing density the radiation pattern changes its character completely: the resonance cones vanish and a single, narrow (3 dB width $\sim$ 14°) beam is radiated along the field lines on-axis with the dipole. In the high density regime the receiving antenna is in the far-zone ($\rho > 3\lambda_{||}$) but the effective antenna length has also increased. By comparing the radiation pattern for a long (5 cm) and a short dipole (1 cm) one can observe the cone structure for the short dipole to higher densities than for the long dipole and thereby conclude that the electric dipole length is most crucial to the shape of the antenna radiation pattern. Since the receiver gain is constant in Figure 4 one can also see increased damping at higher densities.

2.1.2 Polarization Measurements

In the small amplitude regime the wave polarization has been checked at both low and high densities. After verifying that the dipole has an amplitude dependence $E \sim \cos\alpha$ in vacuum (Figure 5a) one finds that on the resonance cone (Figure 5b) the electric field has both components transverse and longitudinal to the cone surface ($E_{\text{long}}/E_{\text{trans}} \approx 1/3$). No amplitude null is obtained for any angle α. When the exciter dipole is rotated around its axis ($||\underline{B}_0$) one finds again a perfect null at $\beta = 90°$ in vacuum, but only an amplitude minimum ($E_{\text{min}}/E_{\text{max}} \approx 0.35$) on the resonance cone. Thus the polarization is elliptic and the cone, although weaker, exists also in the H-plane of the dipole.

In the high density regime the polarization has been measured as indicated in

Figure 6. The axial interferometer traces (bottom) show phase shifts but no amplitude variation with dipole polarization indicating circular polarization. By following a stationary phase point, for example a maximum where the dipole is aligned with the local electric field, one notices that the $\underline{E}$ vector rotates around the magnetic field lines in a right-hand corkscrew motion. Thus the wave is right-hand circularly polarized.

2.1.3 Nonlinear Effects

Figure 7 shows again the variation of the dipole radiation pattern with density, but now in an afterglow plasma ($kT_e \approx 0.3$ eV) at both large (Figure 7a) and small (Figure 7b) amplitudes. Although the transition from the resonance cone to the narrow-beam pattern is visible in both cases the amplitude behavior is entirely different. While at small amplitudes the wave damping strongly increases with density, it decreases with ω_p/ω in the nonlinear regime. The large amplitude high density radiation pattern is narrower (3 dB width ≈ 12°) than in the linear regime. Furthermore, with increasing axial distance from the exciter up to $20\ \lambda_{||}$ the radial width of the field pattern and the amplitude do not change significantly. This self-ducting of a large amplitude whistler wave has been described in an earlier report.[5]

Figures 8 and 9 show that the nonlinear effects are different at small and large densities. In the resonance cone regime (Figure 8b) increasing applied rf power to above $P_{rf} \approx 10W$ creates low frequency fluctuations in the plasma which fill the entire plasma column. For $10W < P_{rf} < 50W$, the cone amplitude increases less than proportional with applied rf voltage (see Figure 9), presumably due to energy transfer into instabilities. The origin of the reduced fluctuations has so far not been investigated. The shape of the radiation pattern is not changed significantly.

However, at high densities nonlinear effects become noticeable at very small rf amplitudes ($V_{rf} \gtrsim 5$ volt). The received signal first rapidly increases with applied rf amplitude, then grows linearly and finally saturates when again low frequency fluctuations are generated. The width of the radiation pattern narrows in the nonlinear regime; only at the highest available power levels ($P \gtrsim 100W$) a broadening is observed.

2.2 Magnetic Loop Antenna

2.2.1 Resonance Cones

At moderate densities ($\omega_p/\omega < 10$) the radiation pattern of the radial magnetic loop (Figure 2 top) exhibits also a resonance cone pattern (Figure 10a). The magnetic field of the loop antenna is orthogonal to the static $\underline{B}_o$ field; the signal is detected with the vertical electric dipole. The dependence of the resonance cone angle θ_c on normalized magnetic field ω/ω_c is shown in Figure 10 at small rf amplitudes. At high densities the theoretical relation becomes density-independent as shown below:

$$\sin^2\theta_c = \frac{\omega_p^2/\omega^2 + \omega^2/\omega^2-1}{(\omega_p^2/\omega^2)(\omega_c^2/\omega^2)} \xrightarrow[\frac{\omega_p^2}{\omega^2} >> 1]{} \left(\frac{\omega}{\omega_c}\right)^2$$

The data points fall close to this expected curve (Figure 10b).

The resonance cone pattern has been mapped at different receiver dipole distances ρ. The polar plot (Figure 11a) shows that the cone angle is essentially independent of distance and that the 3 dB half-width ($\rho\Delta\theta_c$) does not increase with distance, in fact, the angular width ($\Delta\theta_c$) decreases with distance. The peak amplitude on the cone decreases like $E \sim 1/\rho$ as shown in Figure 11b, indicating the near-zone electrostatic character of the field distribution.

2.2.2 Polarization, Reciprocity

The magnetic loop can be rotated such that the rf magnetic field $\underline{B}_1$, is either parallel or perpendicular to the static field $\underline{B}_o$. Figure 12a shows that for $\underline{B}_1 \mid\mid \underline{B}_o$ ($\alpha = 90°$) the cone amplitude goes through a minimum ($E_{90°}/E_{0°} \approx 0.35$), no null is obtained at any angle α. When the receiver dipole polarization is varied (Figure 12b) the result is very similar to the case of an electric dipole exciter (Figure 5b): the dominant field component is perpendicular to the cone surface but appreciable parallel field components exist.

The reciprocity between a magnetic loop and an electric dipole antenna is indicated in Figure 13. The upper trace shows the received oscillating magnetic field set up by an electric dipole exciter and the lower trace is the received electric field excited by a magnetic loop. The similarity of the traces shows that at small amplitudes the antennas are reciprocal and that the cone structure is a property of the medium. In the nonlinear regime, particularly at high densities reciprocity is not satisfied.

2.2.3 Density Dependence

With increasing density the resonance cone pattern vanishes and a narrow-beam pattern emerges similar to the case of the electric dipole exciter. Figure 14 shows that the cone structure vanishes, even though the loop diameter is small compared to the parallel wavelength ($d \sim \lambda_{||}/3$). The damping increases with density.

2.2.4 Nonlinear Behavior

The nonlinear properties of dipole and loop radiation pattern are qualitatively the same. Figure 15a shows that at high densities the beam-like radiation pattern is more pronounced at larger than at smaller rf power levels. Nonlinear ducting is also observed with the magnetic loop antenna.

Due to the small cross section of the radiated beam (∿ 1.5 cm dia.) the wave intensity is large and nonlinear wave-particle effects become visible. Figure 15b shows a comparison of the wave amplitude along the magnetic field for small and large applied rf levels. There is a smooth amplitude decay at small powers but an oscillatory amplitude pattern in the nonlinear regime. This behavior is characteristic of trapped particles[6] exchanging periodically energy with the large amplitude wave. These effects will be subject to a later, more detailed investigation.

At applied power levels $P_{rf} > 100$ W the magnetic loop excites low frequency fluctuations (Figure 16b) which broaden the radiation pattern (Figure 16a) and tend to saturate the growth of wave amplitude with applied antenna voltage.

Finally, the nonlinear effects have been investigated over a wide range of frequencies, $0.16 < \omega/\omega_c \leq 1$. Figure 17 shows that self-ducting becomes more and more pronounced as $\omega/\omega_c \to 1$. However, even at $\omega/\omega_c \leq 0.2$ the wave amplitude increases progressively with applied voltage and the radiation patterns become narrower. Side lobes are seen at low frequencies and near $\omega/\omega_c \approx 1$ but they do not scale with ω/ω_c like resonance cones.

3. ANTENNA INPUT IMPEDANCE

Impedance measurements are performed by observing amplitude and phase of the incident and reflected voltages on the transmission line terminated by the exciter antenna (see Figure 18). These signals are obtained from a dual directional coupler connected to the probe terminals, thus the impedance includes the section of transmission line inside the probe shaft. A double time scale sampling technique was developed to measure the complex reflection coefficient. First, a sampling oscilloscope is used to display the high frequency signal. It is convenient to generate a phasor plot by displaying the in-phase and quadrature component of the rf signal on the X and Y axis, choosing a fixed sampling time with respect to the rf period. Since the plasma is pulsed the oscilloscope outputs are sampled at the desired discharge time with two boxcar integrators, averaged over many periods and plotted on an X-Y recorder.

A typical example of such measurements for an electric dipole is shown in Figure 19. The relatively small reflection coefficient in the absence of plasma is due to cable losses and radiation into free space. In the presence of plasma the reflection coefficient decreases and the reflected signal is delayed by $\phi \approx -\pi$. The difference in the absorbed powers ($\Delta P_{abs}/P_{inc} = .37^2 - .31^2 \approx 0.041$) represents the power delivered to the plasma. The phase shift shows the reactive loading of the antenna by sheath and plasma currents. Both phase shift and absorbed power depend on frequency, plasma parameters, rf power level, type of antenna and polarization. Examples for the electric dipole and magnetic loop are given below.

3.1 Electric Dipole

Although the complex reflection coefficient measurements as described above gives the most detailed information one can obtain a faster result by displaying incident and reflected signals vs time while the plasma is pulsed. In order to provide phase information the rf signals are heterodyned with a common local oscillator to a very low intermediate frequency ($\omega_{LO} - \omega_{signal} \approx 2\pi \times 5\text{kHz}$) and the waveforms are displayed on a dual trace oscilloscope.

Figure 20 shows on the top trace incident and reflected signal when the transmission line is disconnected from the antenna and left open. Total reflection yields $V_{refl.} = V_{inc}$. In the second case the line is matched with a 50Ω termination; now the VSWR is $(V_{inc} + V_{refl})/(V_{inc} - V_{refl}) \approx 1.05$ and the reflected power is $P_{refl}/P_{inc} \approx 6\text{x}10^{-4}$. The third trace shows the axial dipole antenna in the absence of plasma. Approximately half of the incident power is absorbed in the 3m-long high temperature coaxial cable, the balun transformer, stainless steel dipole, and a small fraction is radiated into space. The fourth trace indicates the dipole loading by the plasma. For reference the discharge current is displayed at the bottom; there is a small constant current flow of approximately 5A which is increased to 200A during the pulse. Even the low density background plasma prior to the pulsed discharge improves the dipole matching ($P_{refl}/P_{inc} \approx 0.32$), but especially during the build-up of the pulsed plasma the antenna loading is very pronounced ($P_{refl}/P_{inc} \approx 0.14$); approximately 36% of the incident power is absorbed by the plasma. During the discharge and early afterglow this value drops to 23%. How much of this power is radiated into the far zone may be roughly estimated as follows:

The calibrated magnetic loop indicates a wave magnetic field $B_1 \approx 34 \times 10^{-3}$G for an applied power $P_{inc} = 6.1$W. The field distribution has a cross section of $A \approx 20$ cm^2 so that under the assumption of plane TEM waves the radiated power is given by

$$P_{rad} = 2A \frac{1}{n} \eta_o H^2$$

where $n = \lambda_o/\lambda_{||} \approx 50$ is the refractive index, $\eta_o = \sqrt{\frac{\mu_o}{\varepsilon_o}} = 377\Omega$ is the free space impedance and the factor of 2 takes radiation into both directions along $\underline{B}_o$ into account. With the above values one obtains $P_{rad} = 0.22$W or 3.6% of P_{inc} as compared to $P_{abs} = 1.4$W. Due to the assumed simple relation between E and H and the actual duct-like radiation pattern, the estimate is too crude to draw conclusions from it.

3.2 Magnetic Loop

A similar impedance measurement for the radial magnetic loop is shown in Figure 21. The absorbed power during the discharge is found to be $P_{abs}/P_{inc} = 0.846^2 - 0.754^2 = 0.147$. In order to check whether this power is radiated by whistler waves, two important parameters have been varied as shown in Figure 22. When the magnetic field is decreased such that $\omega/\omega_c > 1$ the reflected power increases by 10% (Figure 22a). When the wave magnetic field is aligned parallel to the direction of wave propagation the power reflection again increases by 10%. Thus one can conclude that the enhanced absorption of approximately 10% under favorable conditions for whistler wave propagation corresponds to radiated power.

Finally, Figure 23 shows that in the low density regime where the loop excites resonance cones no enhanced absorption is observable to within measurement accuracy ($\delta P_{refl}/P_{inc} \approx 5\%$).

REFERENCES

1. "LAMPS", TRW Systems Group Report 4351.7.74-121, Sept. 1974.
2. R. Limpaecher and K.R. MacKenzie, Rev. Sci. Instrum. 44, 726 (1973).
3. H.H. Kuehl, "Electromagnetic Radiation from an Electric Dipole in a Cold Anisotropic Plasma", Phys. Fluids 5, 1094-1103 (1962).
4. R.K. Fisher and R.W. Gould, "Resonance Cones in the Field Pattern of a Short Antenna in an Anisotropic Plasma", Phys. Rev. Letters 22, 1093-1095, (1969).
5. R.L. Stenzel, "Self-Ducting of Large Amplitude Whistler Waves", submitted to Phys. Rev. Letters.
6. P. Palmadesso and G. Schmidt, "Collisionless Damping of a Large Amplitude Whistler Wave", Phys. Fluids 14, 1411-1417, (1971).

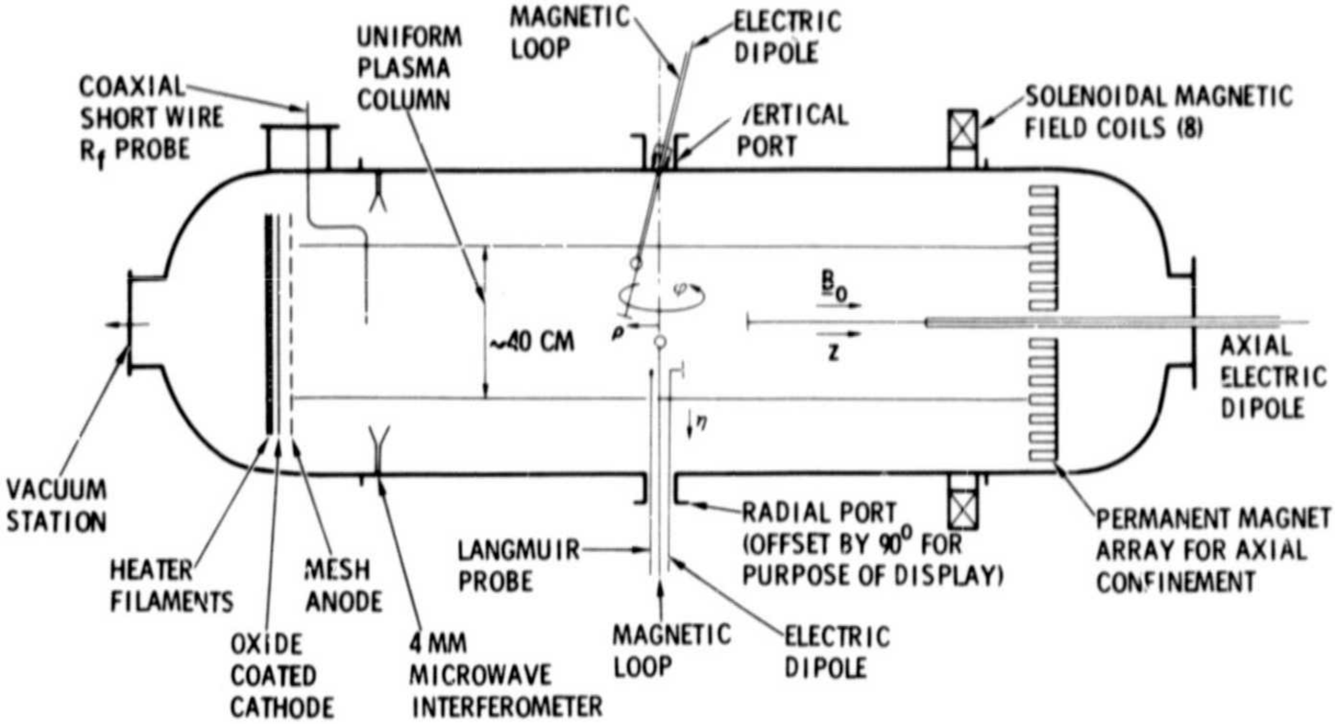

Figure 1. Schematic of the experimental setup

RADIAL MAGNETIC LOOP

VERTICAL ELECTRIC DIPOLE

AXIAL ELECTRIC DIPOLE

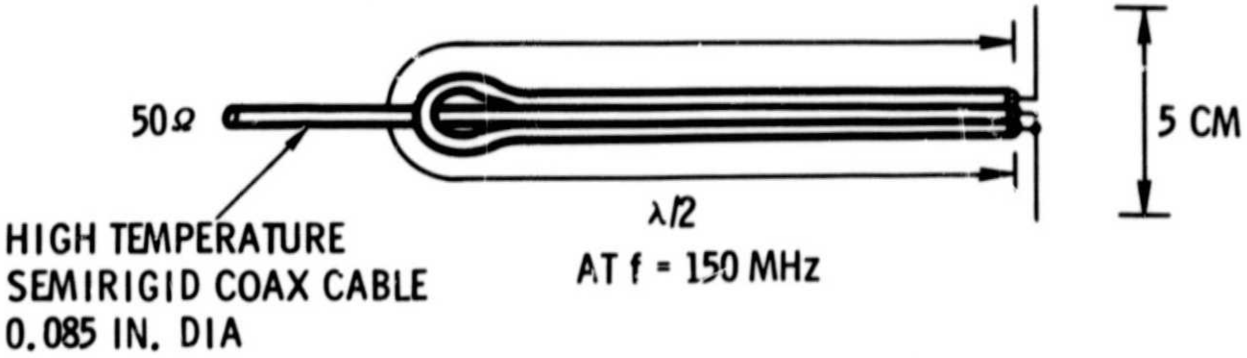

Figure 2. Sketch of the antennas investigated.

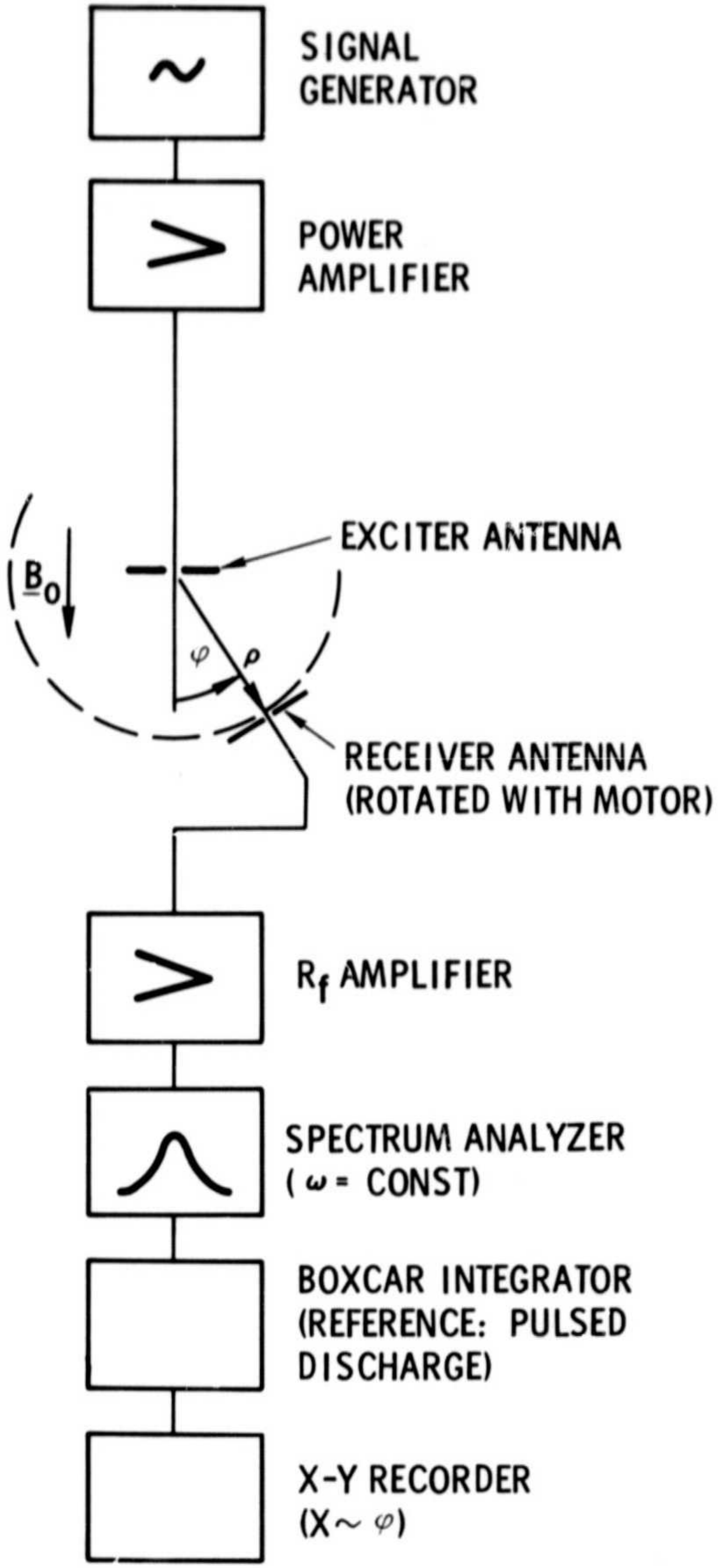

Figure 3. Block diagram for measuring antenna radiation patterns (Amplitude vs angle ϕ) in a pulsed plasma.

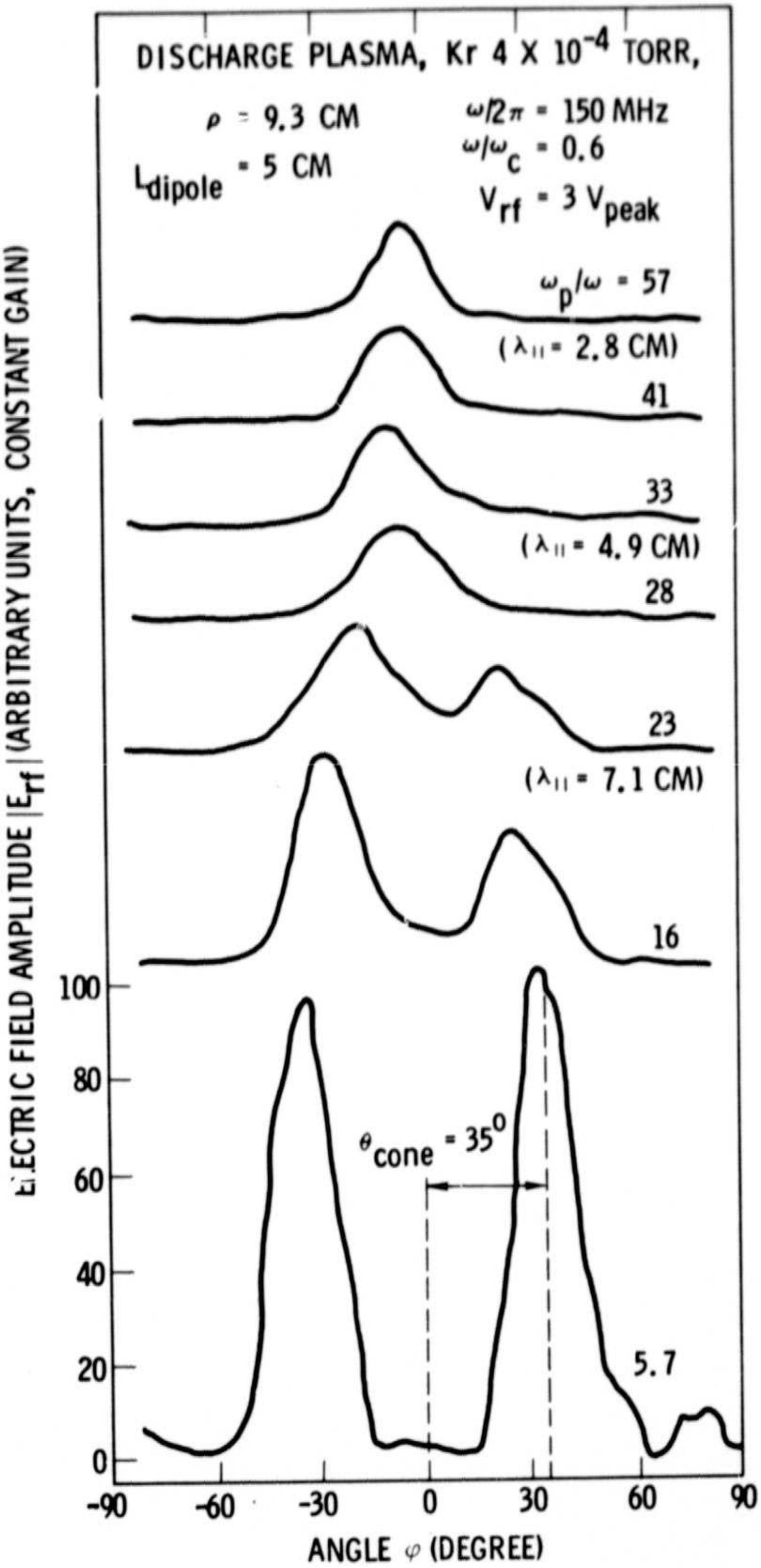

Figure 4. Antenna radiation pattern of the axial electric dipole at different densities. The left hand scale applies to all curves.

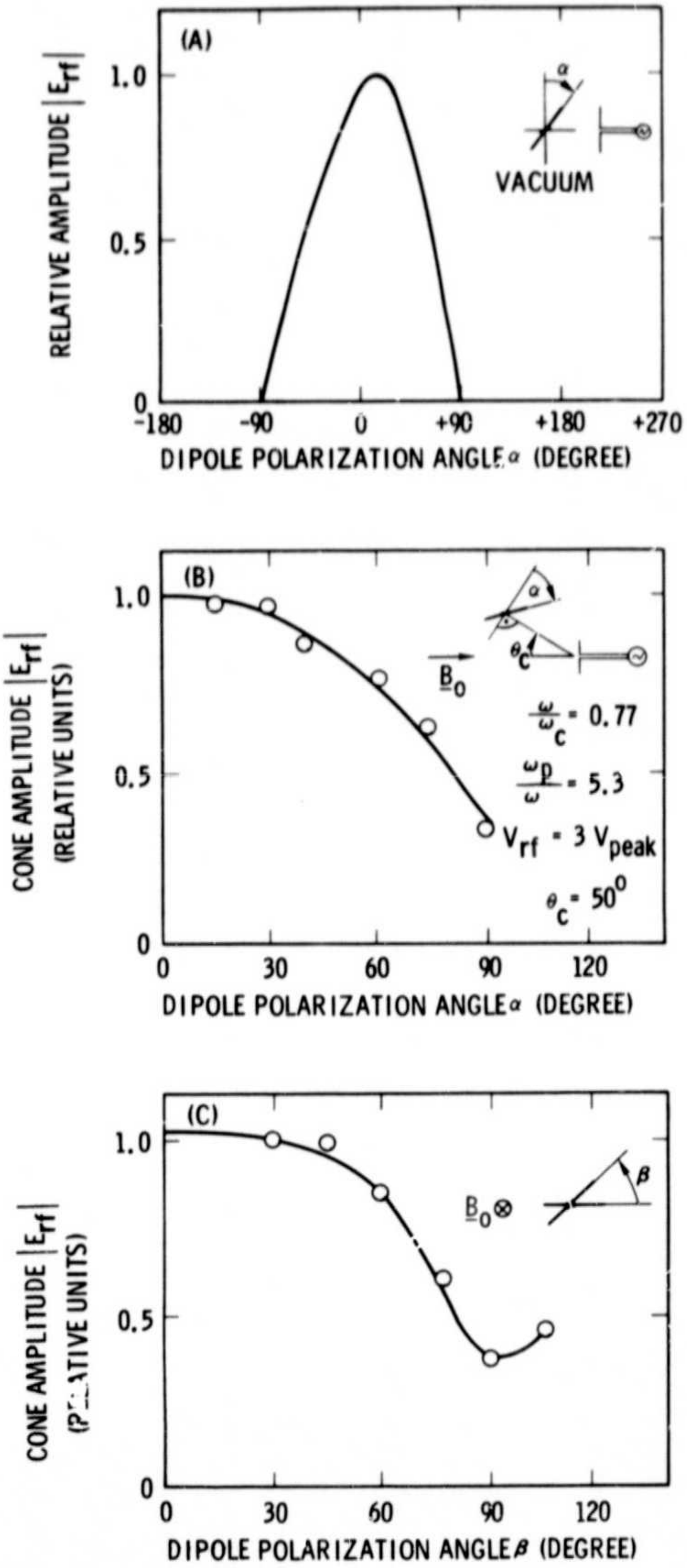

Figure 5. Field polarization measurements on the resonance cones.

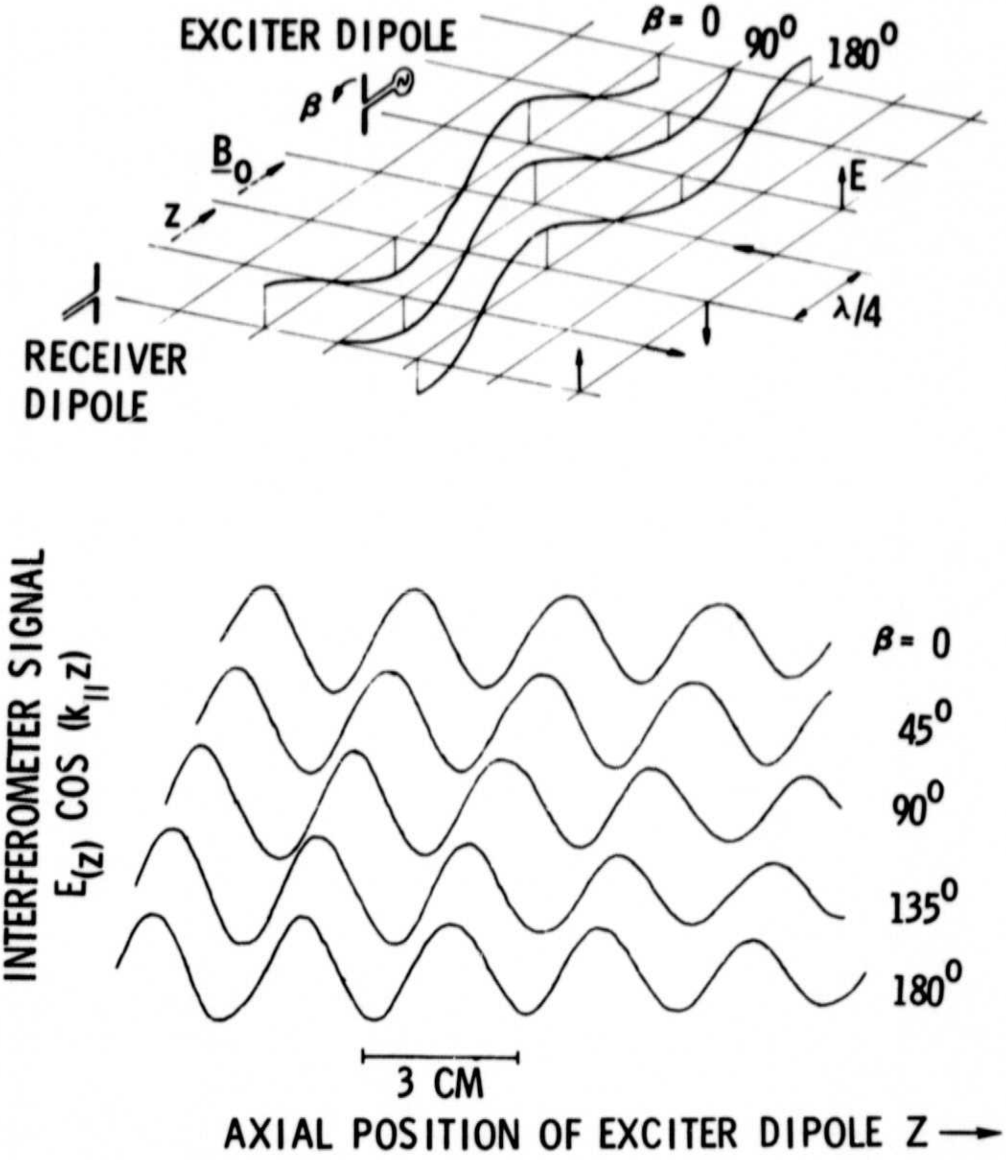

Figure 6. Polarization measurements (principle sketched on top) of small amplitude whistler waves verify right-hand circular polarization.

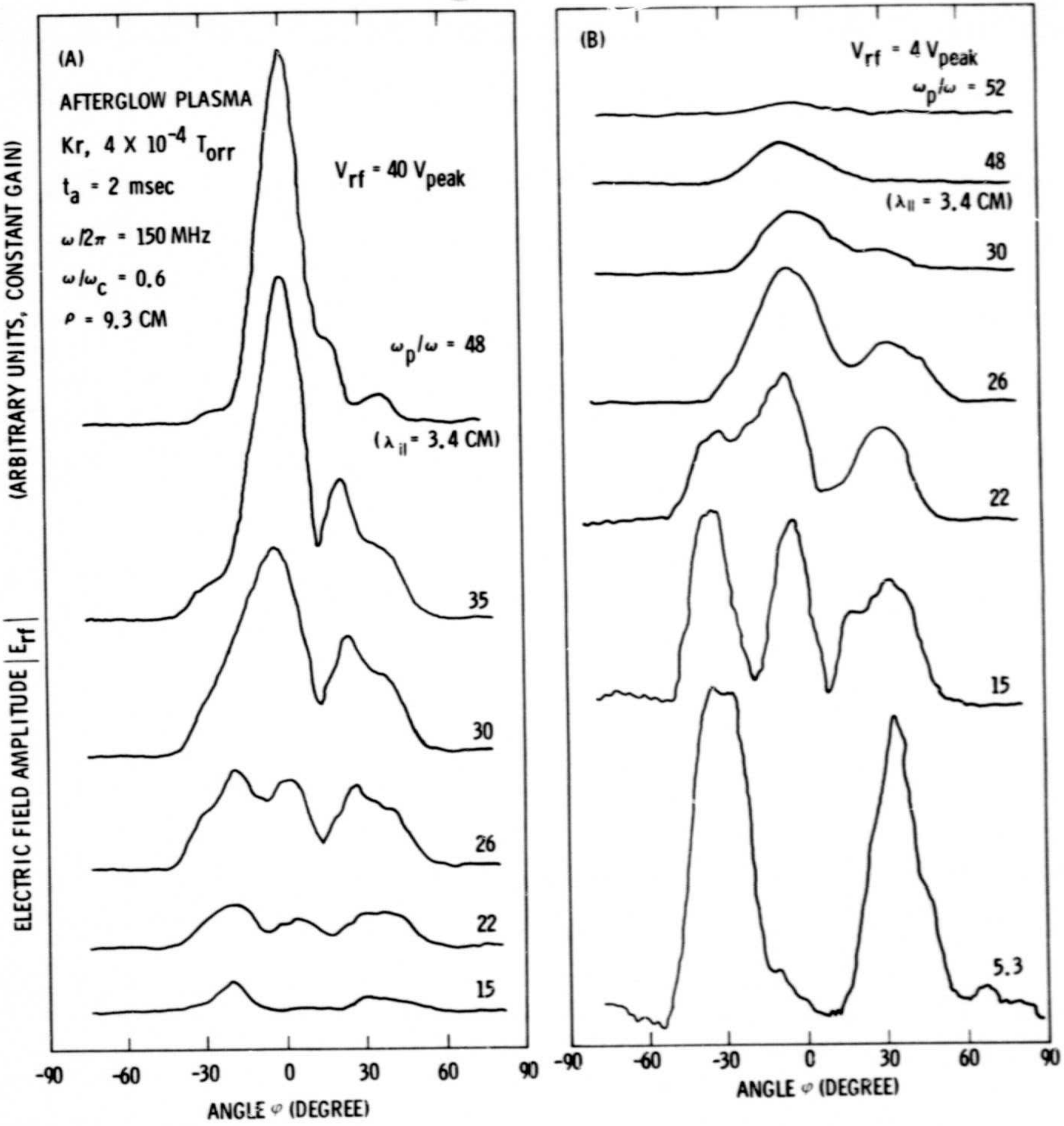

Figure 7. Dipole radiation patterns at different densities in the linear (B) and nonlinear (A) amplitude regime.

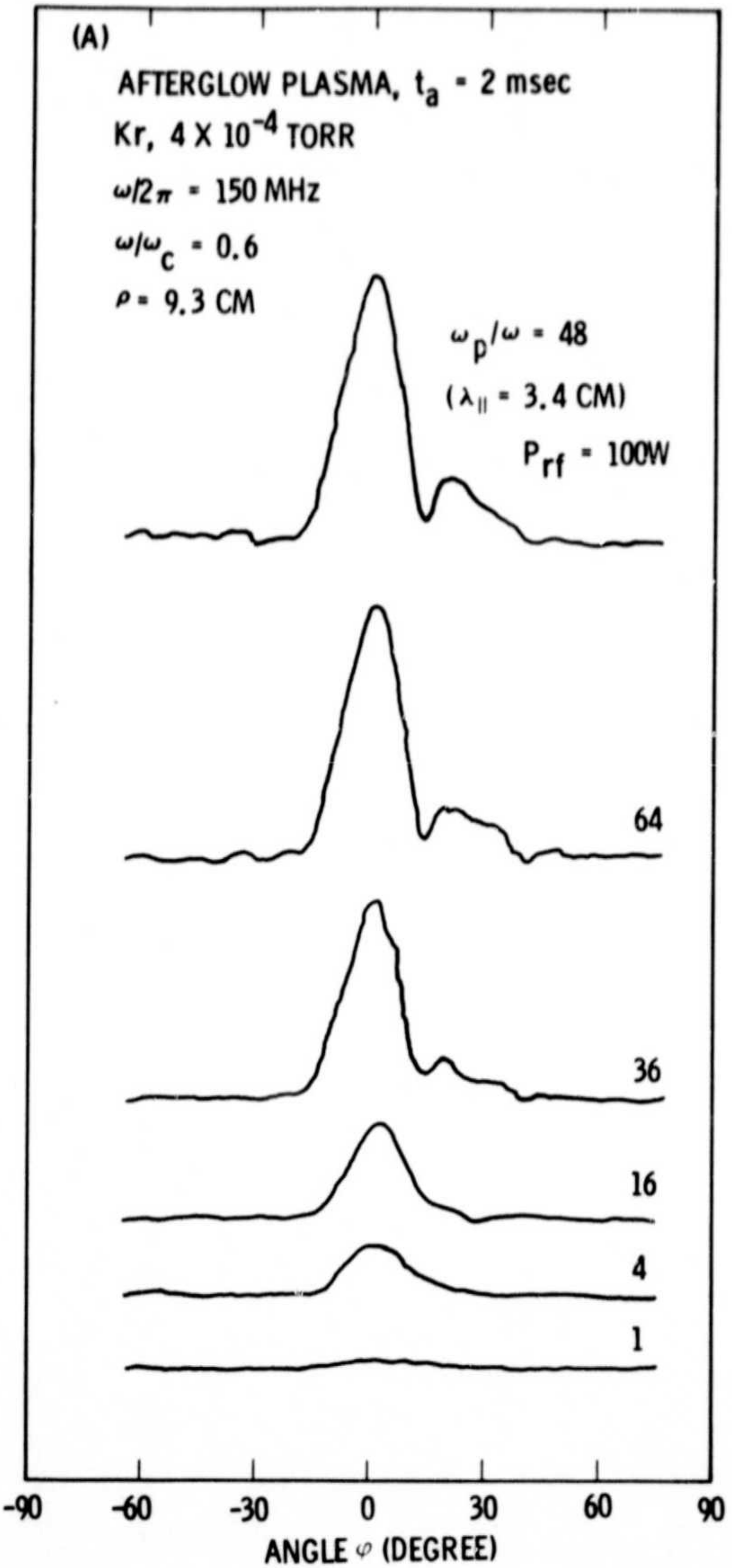

Figure 8a. Dipole radiation patterns at increasing rf power levels in the high density (A) and low density (B) regime.

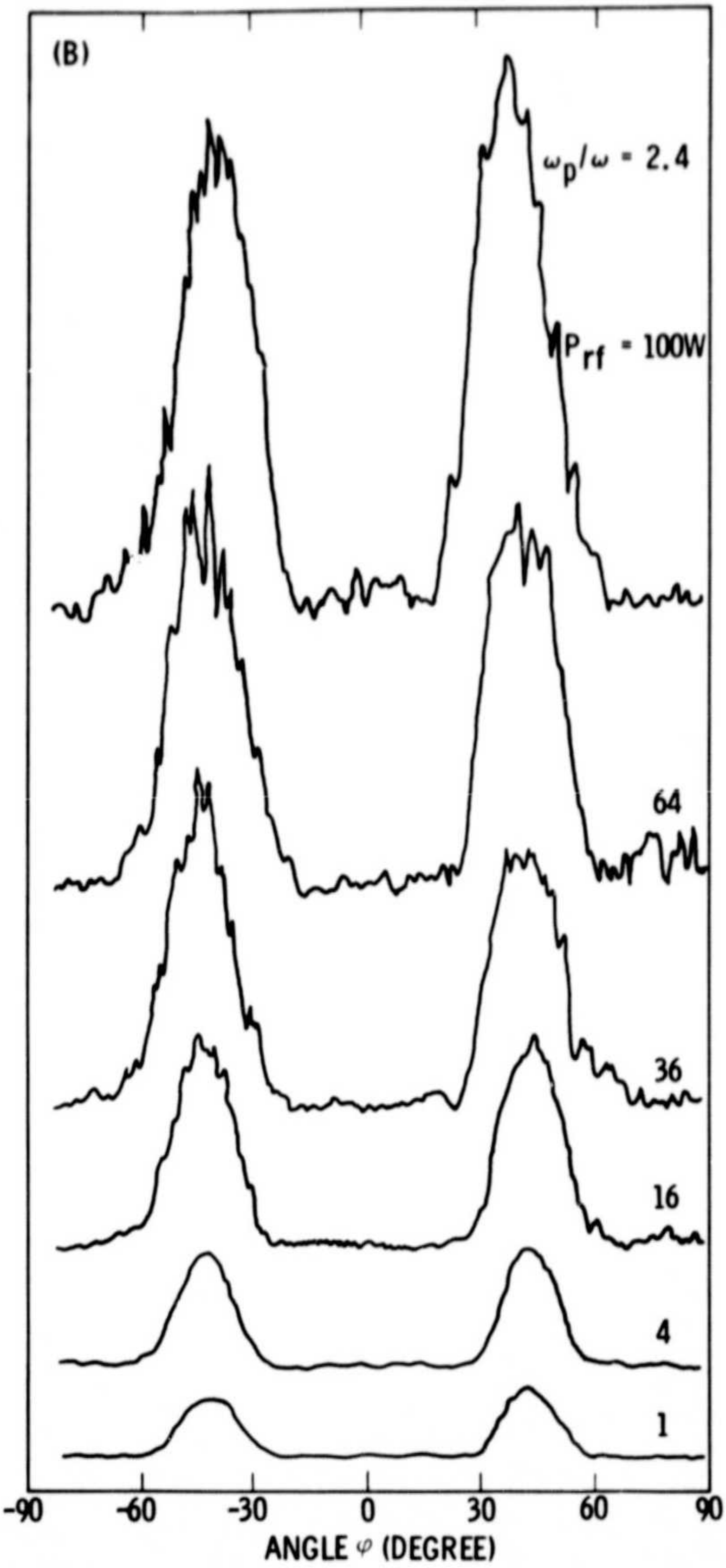

Figure 8b. Dipole radiation patterns at increasing rf power levels in the high density (A) and low density (B) regime.

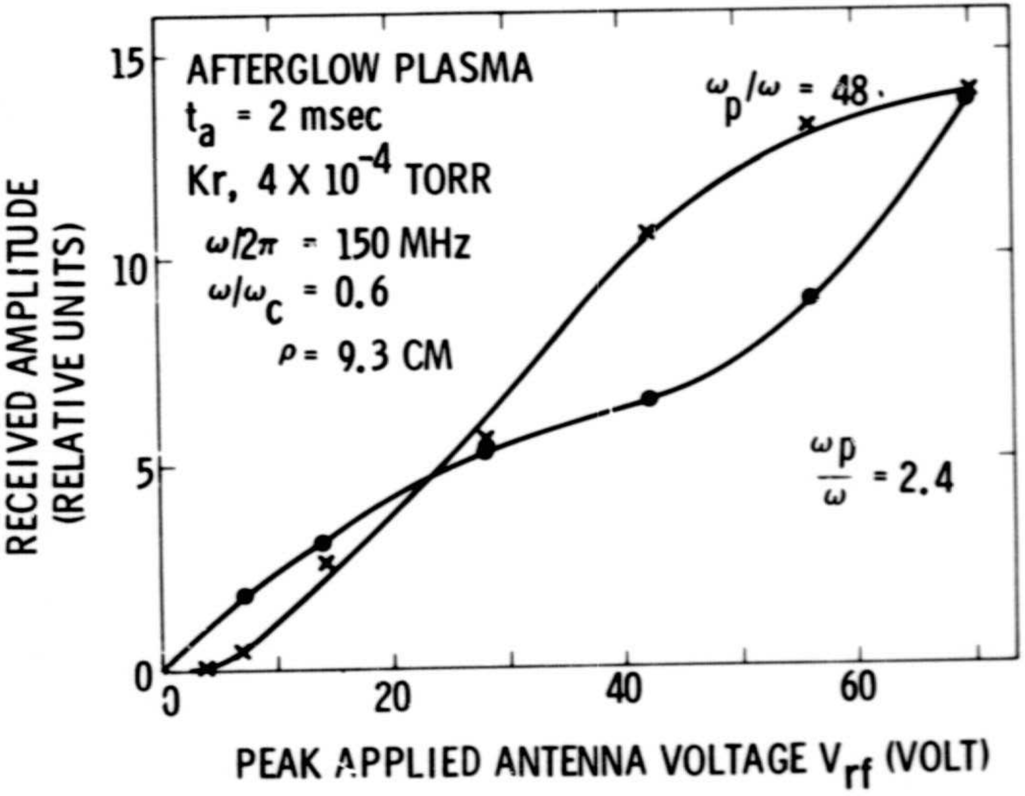

Figure 9. Wave amplitude vs applied antenna voltage in the low density (dots) and high density (crosses) regime. The linear regime ends at $V_{rf} \leq 5$ volt.

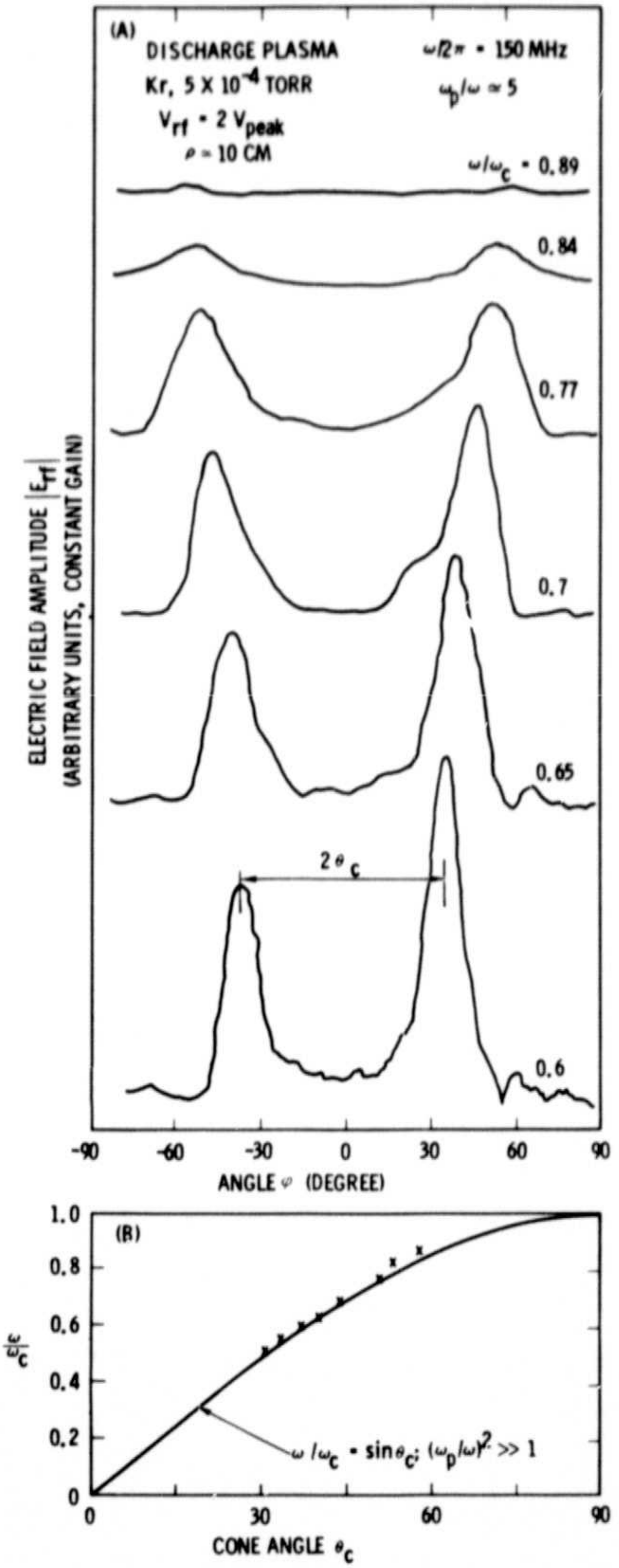

Figure 10. Magnetic loop radiation patterns at different ω/ω_c indicating resonance cone structures.

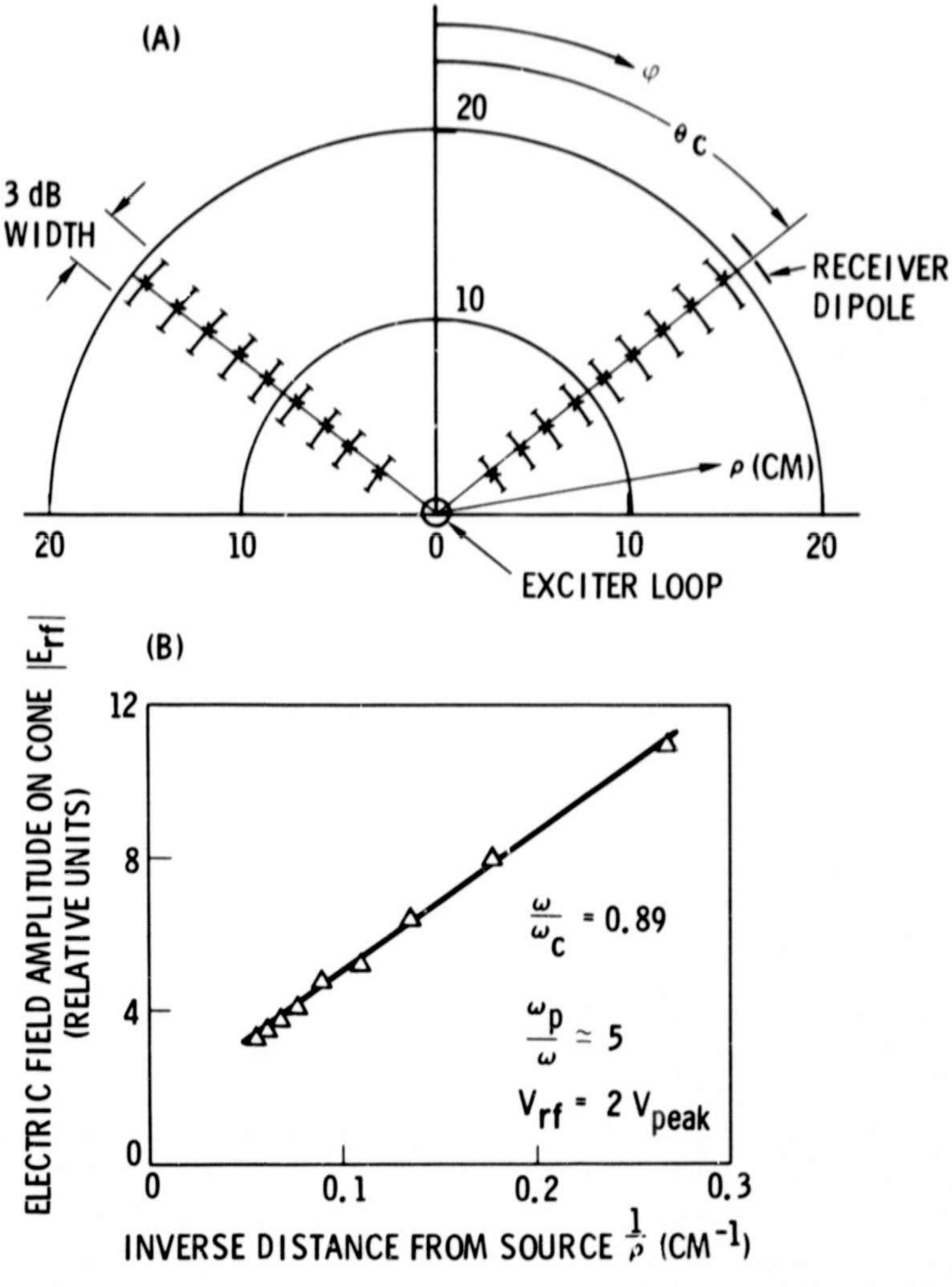

Figure 11. Polar plot of the resonance cones (A) and amplitude behavior along the cone (B).

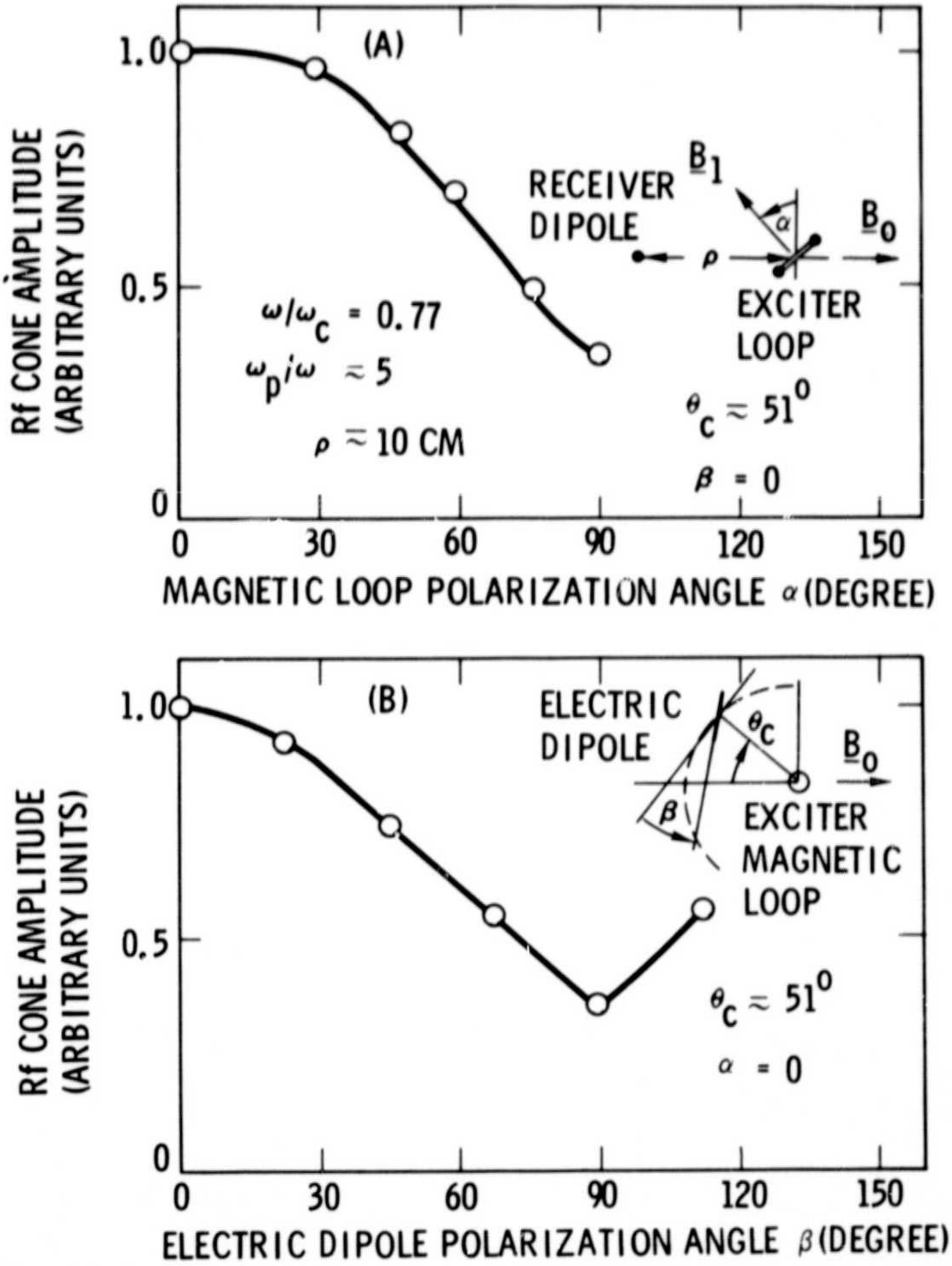

Figure 12. Polarization measurements of loop-excited resonance cones.

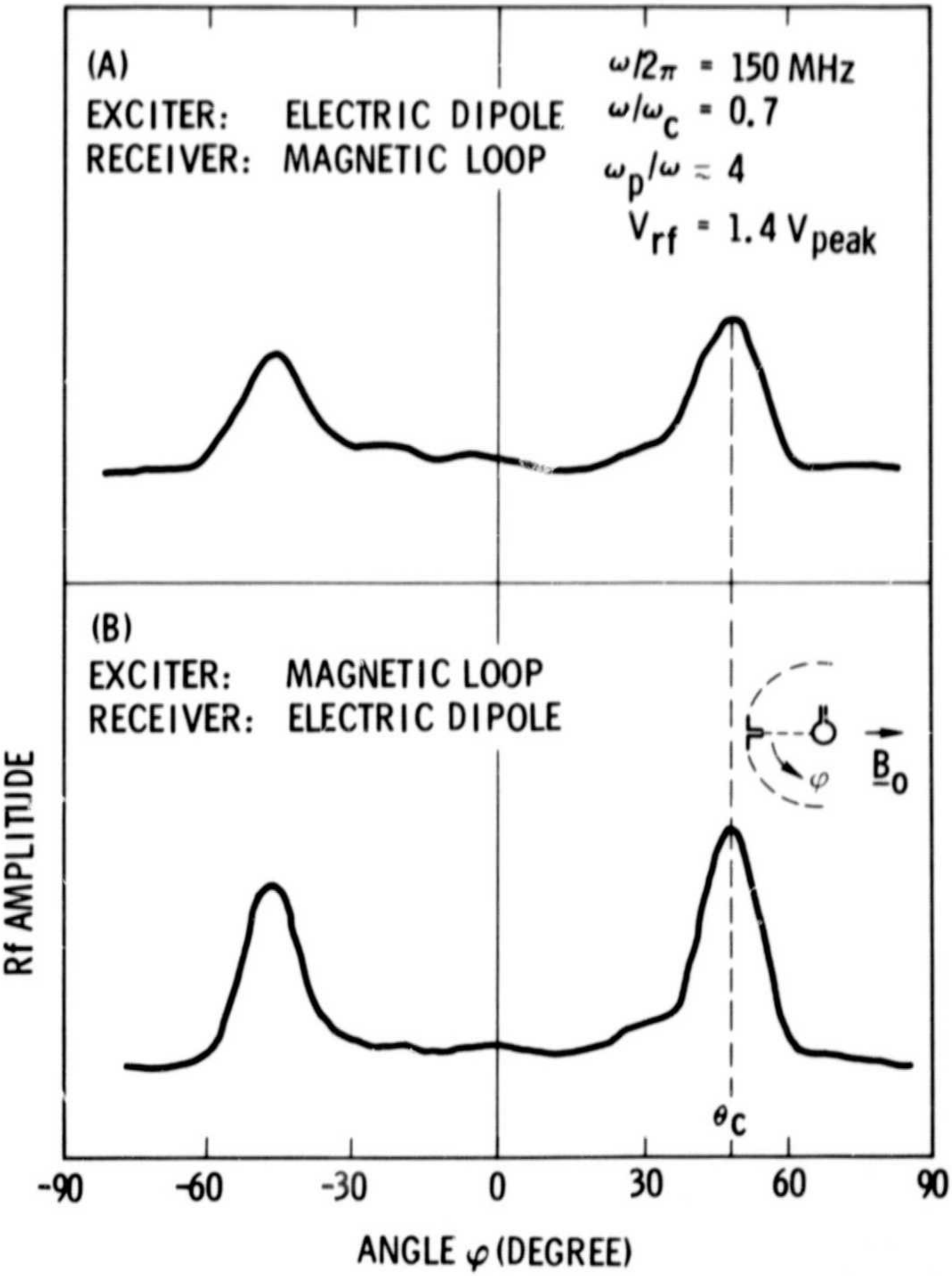

Figure 13. Reciprocity between magnetic loop and electric dipole at small rf amplitudes.

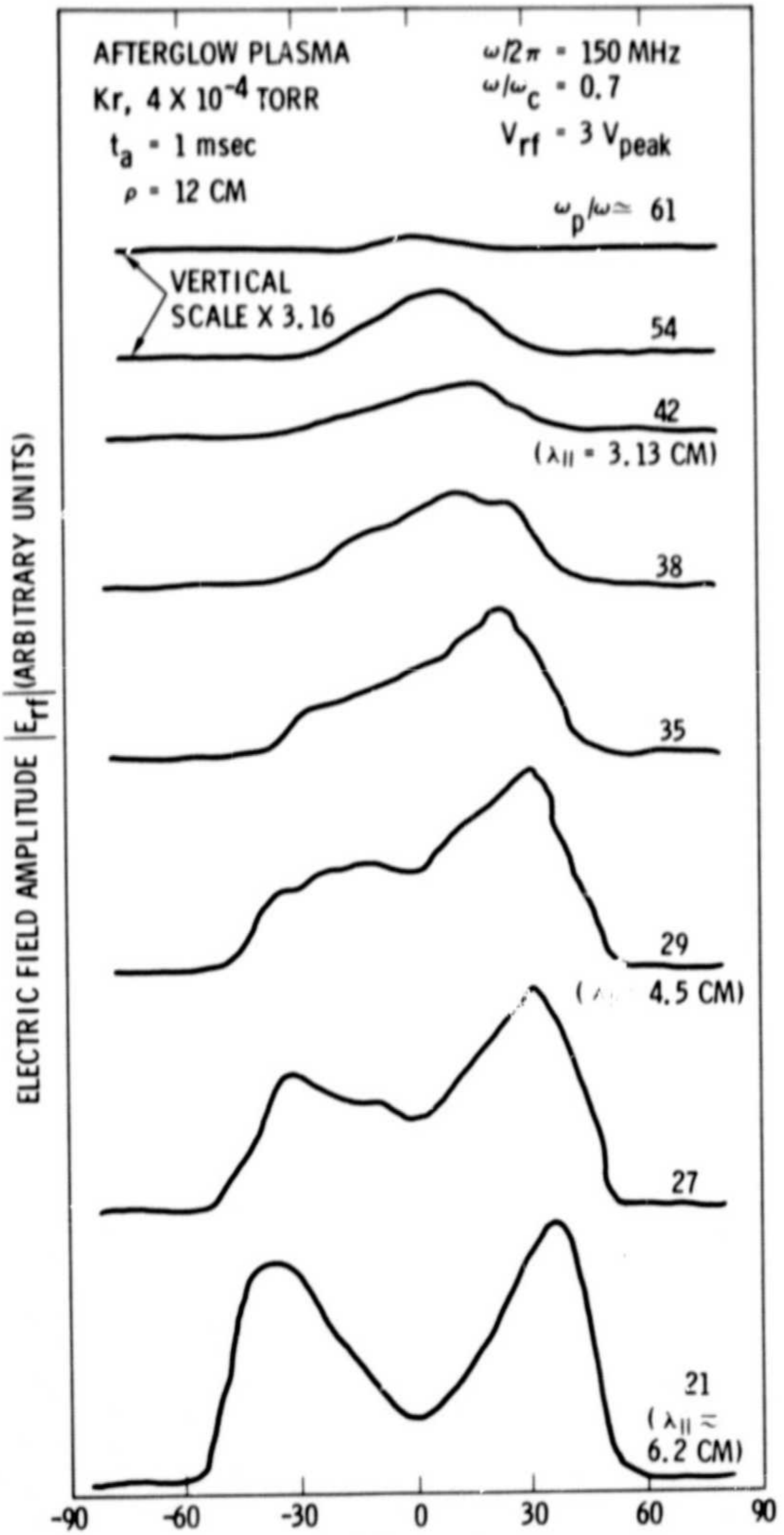

Figure 14. Transition of the loop radiation pattern from low to high densities.

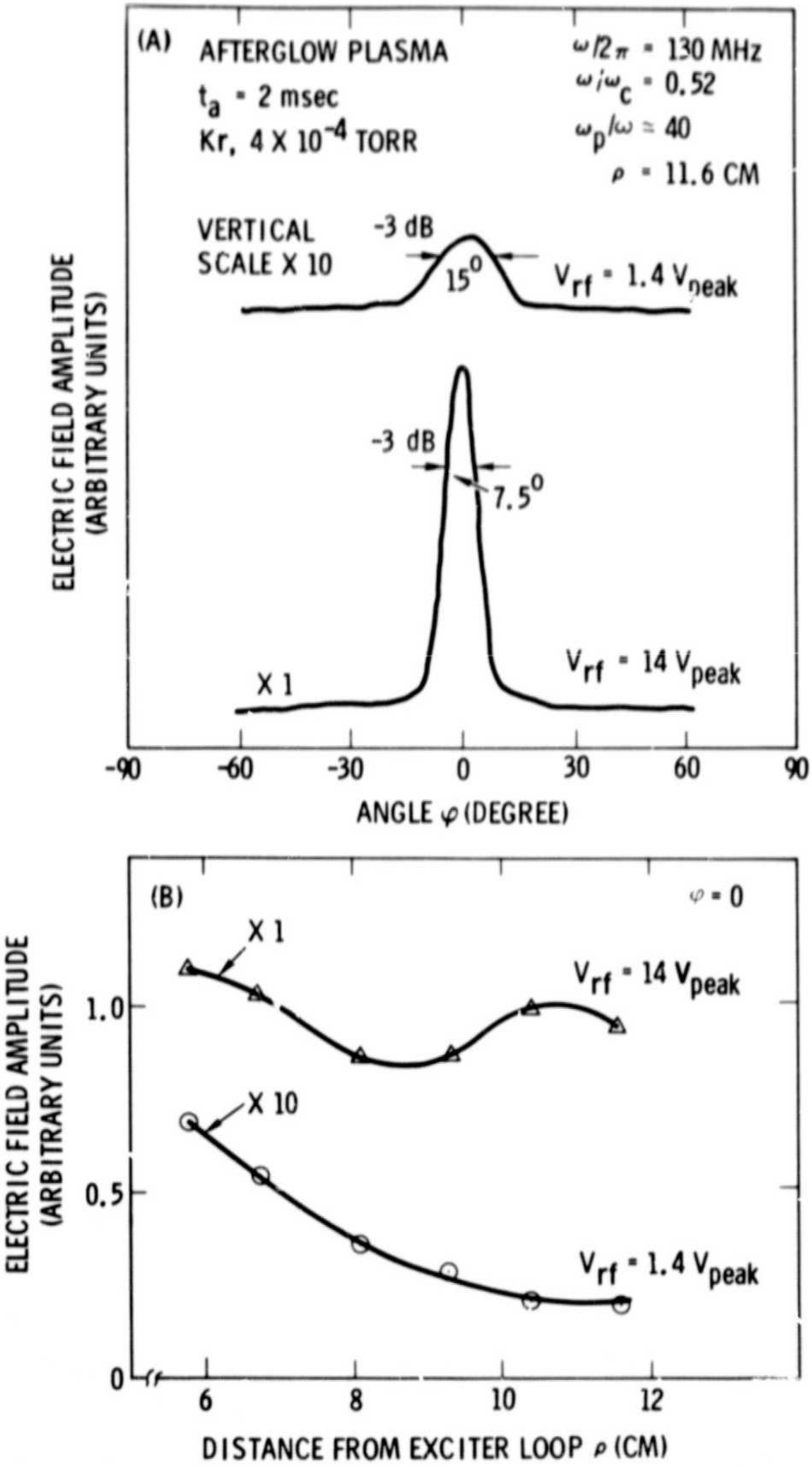

Figure 15. Loop radiation pattern for high densities at small and large rf powers (A) and amplitude behavior along the field (B).

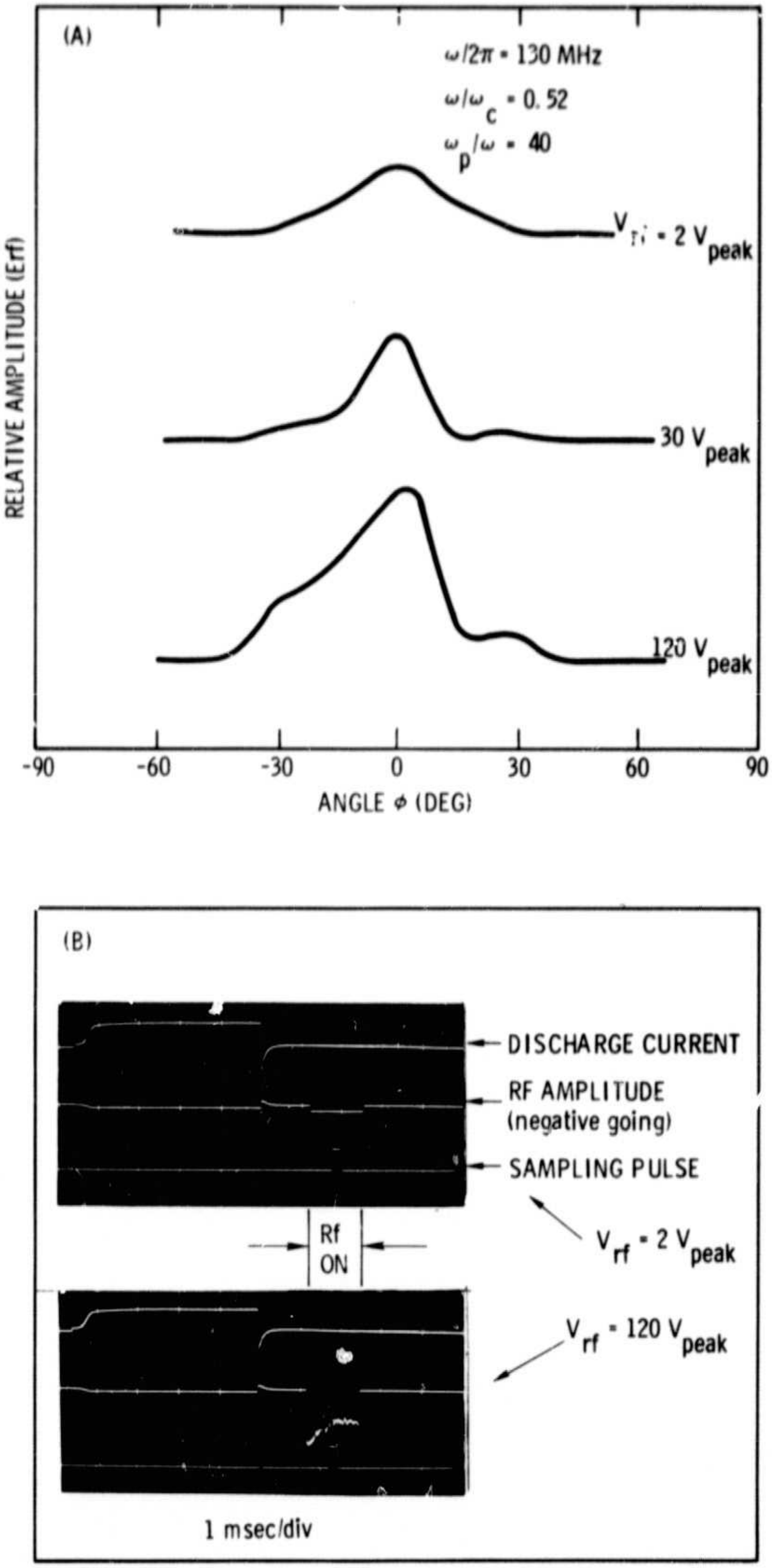

Figure 16. Excitation of low frequency fluctuations (B) at high power levels cause a rebroadening of the radiation pattern (A).

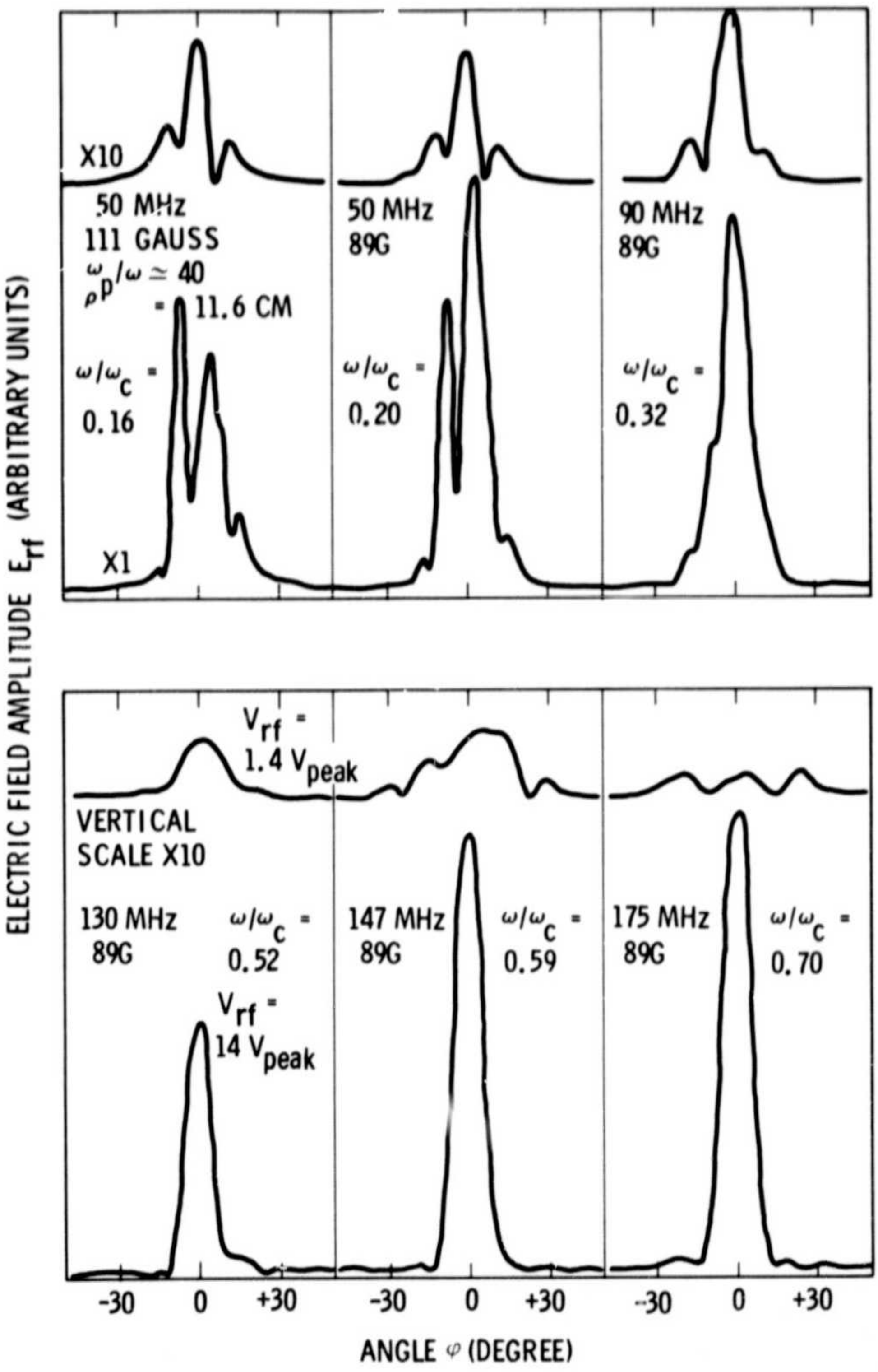

Figure 17. Comparison between small amplitude (top) and large amplitude (bottom) loop radiation patterns at different normalized frequencies ω/ω_c. Note that the scale is changed by the same ratio as the applied rf voltage.

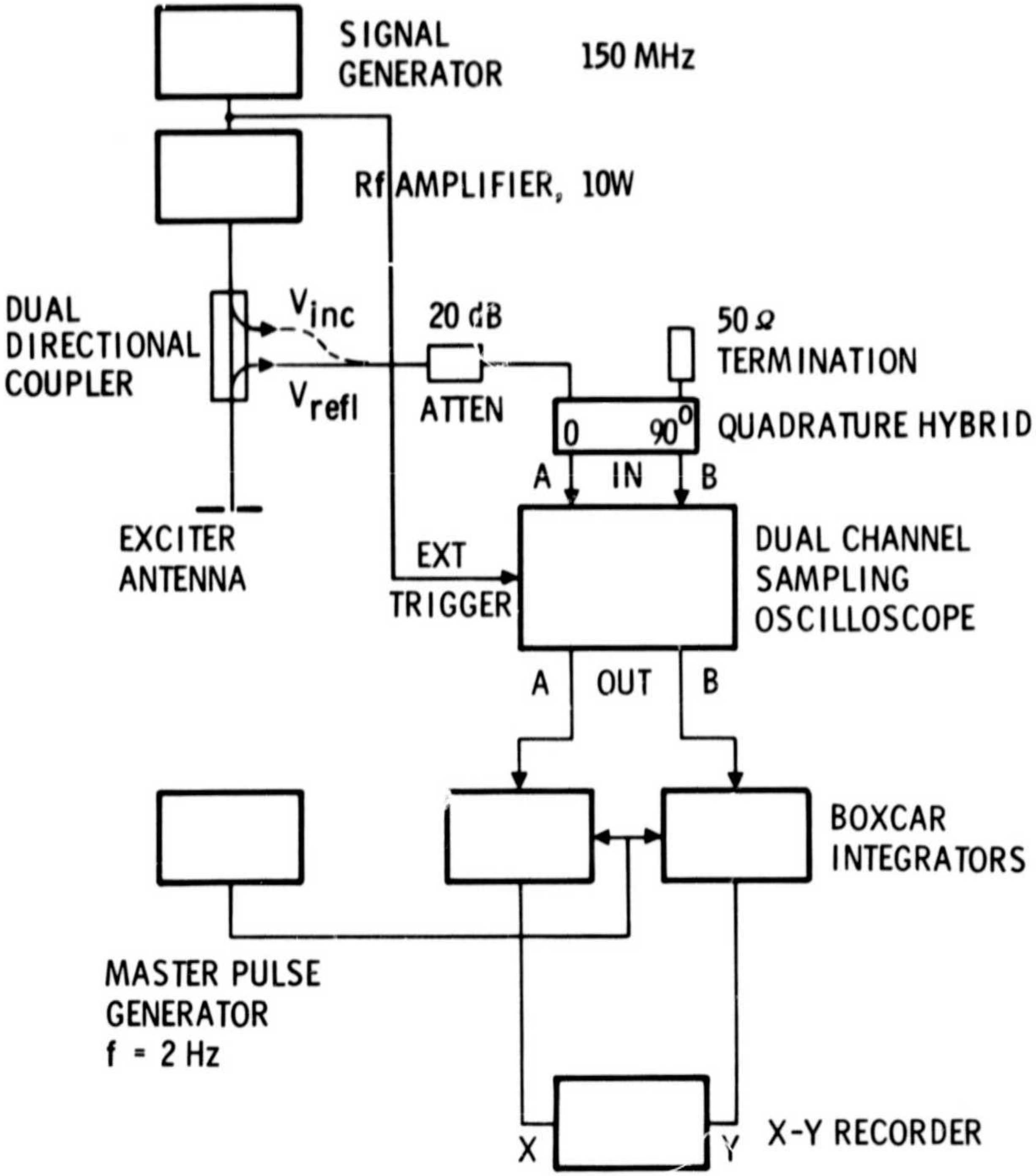

Figure 18. Block diagram for measuring complex reflection coefficients in a pulsed plasma.

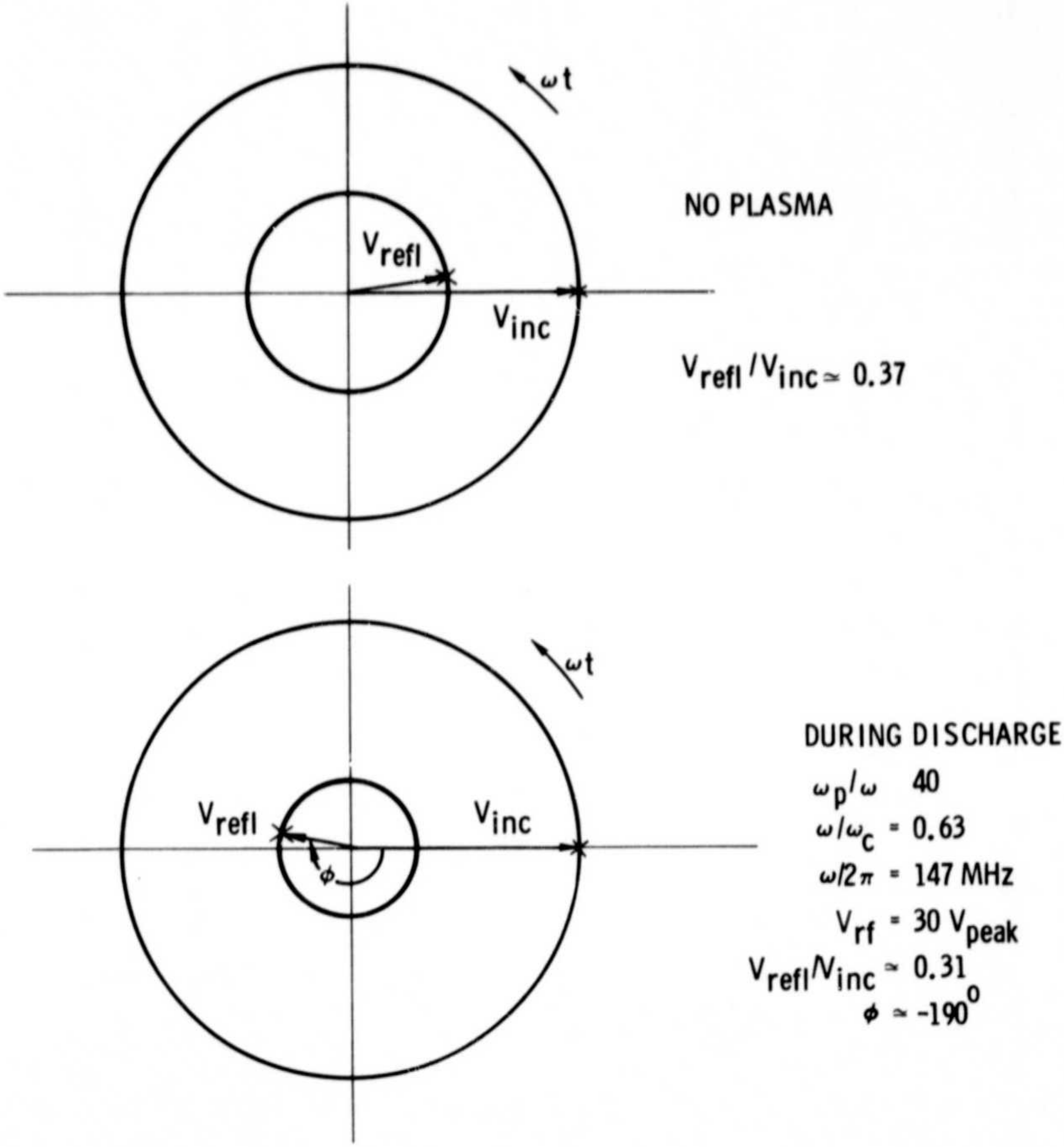

Figure 19. Dipole reflection coefficient in the absence (top) and presence (bottom) of plasma. The data include the lossy transmission line.

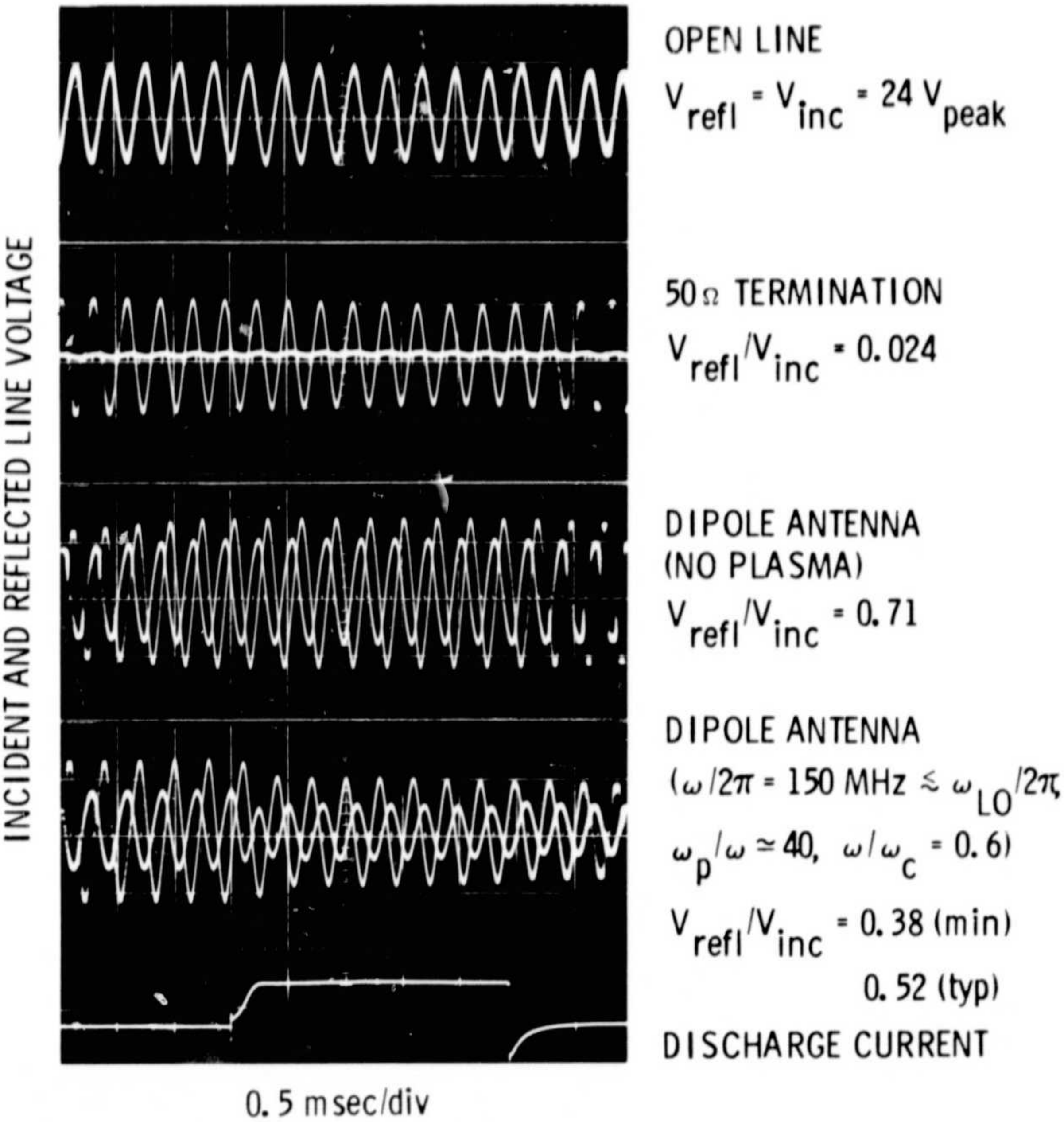

Figure 20. Incident and reflected voltage ($V_{refl} \leq V_{inc}$) vs time under various load conditions.
Note that the signals have been heterodyned to a low frequency so as to show phase shifts.

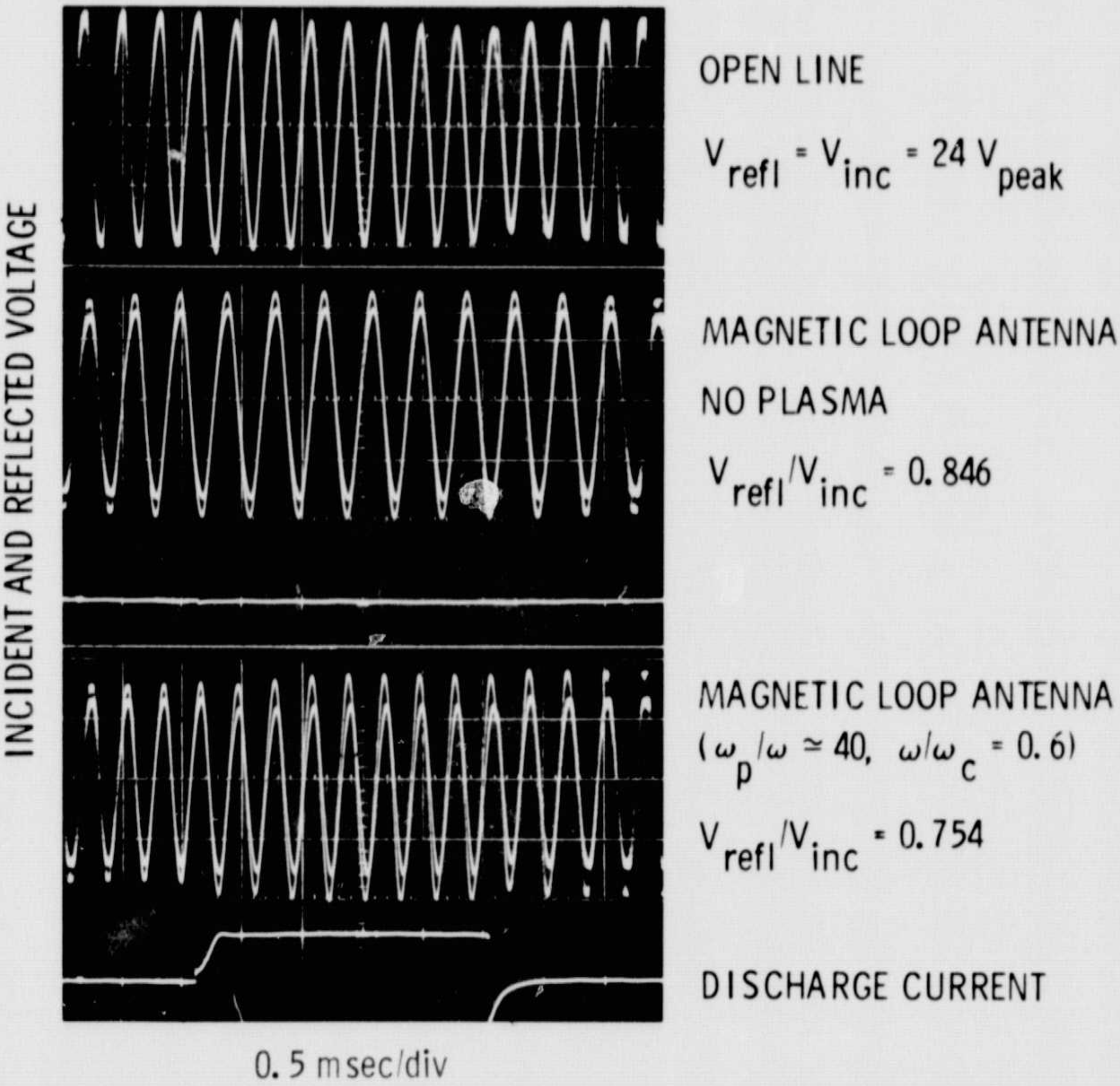

Figure 21. Reflection coefficient measurements for the magnetic loop antenna.

(A) MAGNETIC FIELD DEPENDENCE

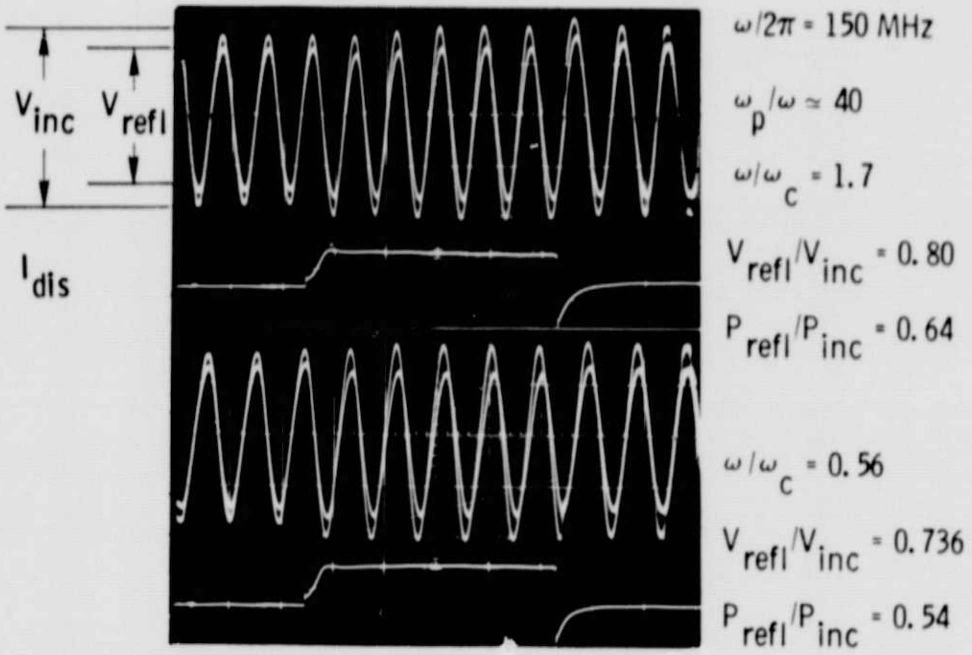

(B) POLARIZATION DEPENDENCE

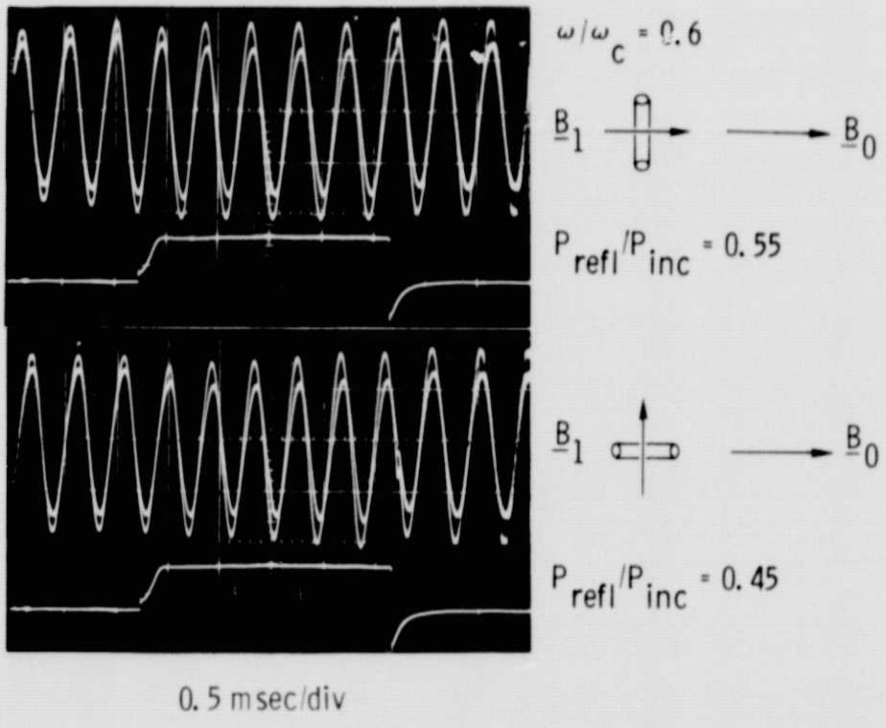

Figure 22. Loop reflection coefficient measurements indicate a 10% increase in absorption due to wave propagation.

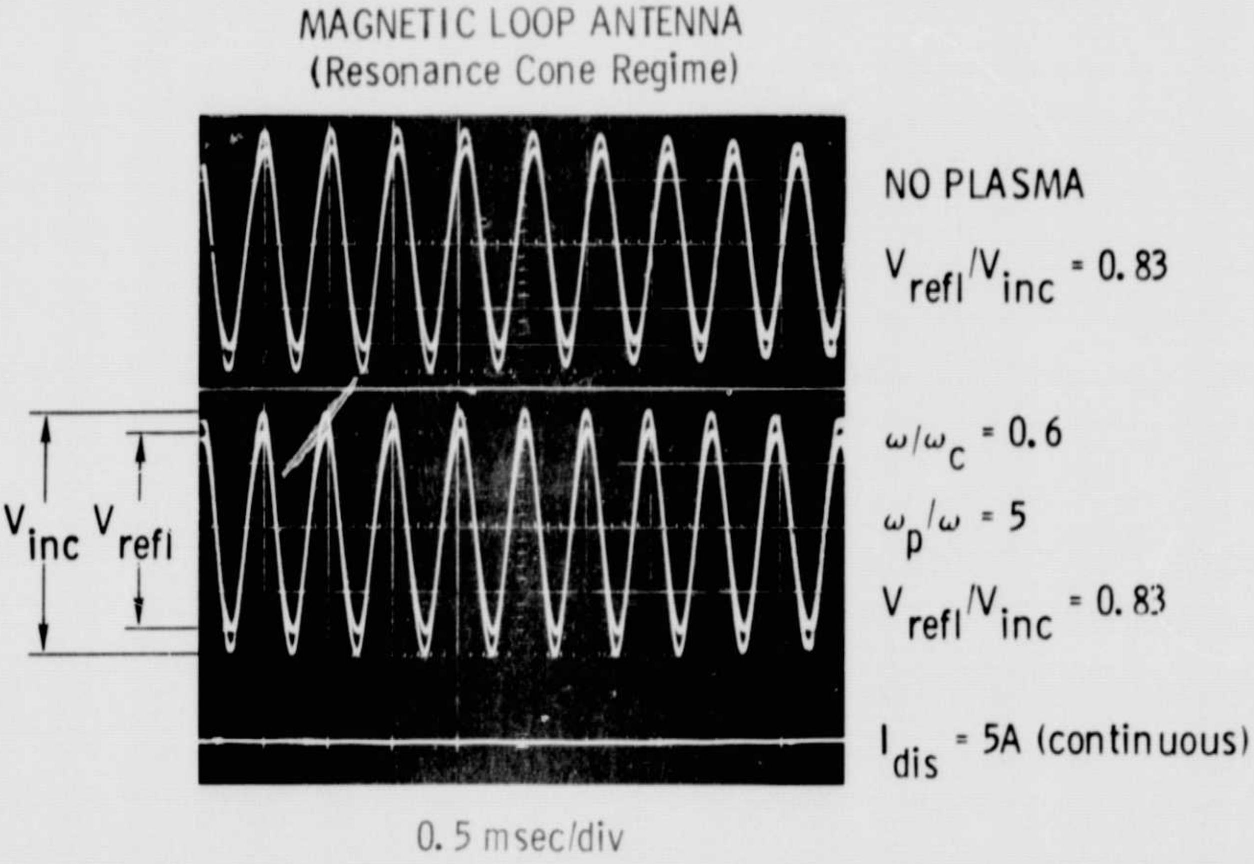

MAGNETIC LOOP ANTENNA
(Resonance Cone Regime)

Figure 23. Loop reflection coefficient measurements indicate no enhanced radiation in the resonance cone regime.

APPENDIX

SELF DUCTING OF LARGE AMPLITUDE WHISTLER WAVES[*]

R.L. Stenzel

TRW Systems, Redondo Beach, California 90278

Abstract

Whistler waves are launched from an electric dipole of length L in a large volume laboratory plasma. With increasing wave amplitude the radiation pattern narrows and finally forms a nearly perfect duct of diameter $d \approx L \approx \lambda_{||}$. The ducted waves propagate without observable damping. The observed nonlinear effects are explained by a wave induced modification of the electron distribution function.

---

[*] Work supported by TRW IR&D funds and NASA Contract No. NAS8-31175.

Currently much attention has been given to the problems of exciting large amplitude Whistler wave from spacecrafts with long wire antennas. The linear wave properties[1] and the behavior of antennas at small amplitudes[2] seem well understood. However, at large amplitudes nonlinear sheath effects, modifications of the plasma by the large amplitude wave and parametric instabilities make a theoretical prediction of the radiation problem very difficult and call for actual experiments. The advantages of scaled laboratory experiments over field experiments in terms of cost, control of parameters, reproducibility and variety of diagnostics are obvious but were so far outweighed by the disadvantage of boundary effects in most small scale laboratory plasmas. We have therefore constructed an unusually large (diameter $\sim 10\lambda_{||}$, length $\sim 100\lambda_{||}$), quiescent, collisionless, magnetized plasma device and investigated the dipole radiation problem at both small and large amplitudes. We observe that with increasing wave amplitude the dipole antenna radiation pattern narrows and eventually collapses into a narrow well collimated duct in which the wave propagates virtually undamped. In the duct the electron distribution function is found to be anisotropic and non-Maxwellian and the density is slightly reduced. The observed instability is qualitatively explained by a positive feedback between wave amplitude and particle anisotropy.

The experiment is performed in a discharge plasma produced in Krypton with an indirectly heated, oxide-coated cathode of diameter d ≈ 50 cm. The plasma column is substantially uniform over 40 cm in diameter (see Fig. 1) and 300 cm in length, has a peak density $n_e \approx 10^{12}\text{cm}^{-3}$, electron temperature $T_e \approx 2\text{eV}$, degree of ionization $n_e/n_n \approx 10\%$, collision rate $\nu_{en}/\omega \lesssim 10^{-3}$ and is uniformly (±0.5%) magnetized with $B_o \approx 100$ Gauss. The discharge is pulsed on for approximately 5 msec with repetition time of 500 msec (see Fig. 2a). Whistler waves of frequency $\omega/2\pi \approx 150\text{MHz}$ are excited with a linear balanced electric dipole (5cm length) movable in axial direction ($\parallel \underset{\sim}{B}_o$) and detected with a short (1 cm) coax-fed wire antenna movable in radial direction. The rf signal is applied in steady state for power levels $P \lesssim 10\text{W}$ and in pulsed mode for $P \lesssim 80W$. The received signal is amplified and applied to an interferometer circuit whose output, $V_{out} \propto E_{(z)}\cos(kz)$, is sampled at a desired time during or after the discharge and then averaged over many events. Plasma diagnostics include Langmuir probes and a 70 GHz interferometer.

We have first verified the small amplitude propagation characteristics. The dispersion relation for the right hand circularly polarized waves propagating along $\underline{B}_o$ is given by

$$k_{||}^2 c^2/\omega^2 = 1 + \omega_p^2/(\omega k v_e)\ Z_+(\zeta_e) \qquad (1)$$

where $\zeta_e = (\omega-\omega_c)/(k_{||}v_e)$ and Z_+ is the plasma dispersion function.^{4} For $|\zeta_e| \gtrsim 3$ the cold plasma approximation $k_{||}^2c^2/\omega^2 \approx 1-\omega_p^2/(\omega^2-\omega\omega_c)$ is valid. In the parameter range $10 < \omega_p/\omega < 25$ and $\omega/\omega_c < 0.75$ we find good agreement with the approximation while for $\omega/\omega_c > 0.75$ thermal corrections according to Equation (1) become noticeable.

The observed wave damping arises from several contributions: (a) Geometric effects. The short dipole launches spherical rather than plane waves; (b) Non-Maxwellian electron disribution functions. The presence of energetic (50eV) electrons during the discharge yields lower damping than in the afterglow where $f_e(v)$ is approximately Maxwellian; (c) Electron-neutral collisions; k_i/k_r increases slightly with neutral pressure; (d) Cyclotron damping dominates as $\omega/\omega_c \to 1$.

The polarization of the wave is determined by rotating the linear exciter dipole around the axis ($|| \underline{B}_o$) and translating it along $\underline{B}_o$ so as to maintain a constant phase at the receiver antenna. The polarization rotates in the same sense as electrons rotate around $\underline{B}_o$. The received amplitude is observed to be independent of dipole rotation thus the wave is right hand circularly polarized.

The large amplitude effects are apparent in Fig. 2b which shows a set of interferometer traces versus time at different power levels applied to the antenna. The probe separation is fixed at approximately $z = 95$ cm, and a constant rf signal is applied in steady state. The oscillations in the interferometer signal,

$E(z)\cos(k_{||}z)$ are due to the increase and decrease of $k_{||}$ with density in the pulsed plasma. The oscillation period has no relation to the Whistler wave period but the oscillation amplitude is directly proportional to the received wave amplitude. At small power levels a number of fringes are seen in the beginning of the discharge where a relatively high concentration of energetic electrons is present. In the afterglow the damping is too high to observe the oscillations with the same sensitivity. However, with increasing power level the waves begin to appear in the afterglow, furthermore, their amplitudes grow in time. Growth rate and saturation amplitude increase with applied power.

The large amplitude Whistler wave gives rise to a nonlinear spatial behavior as indicated in Fig. 3a which shows axial interferometer traces at $t_a = 3$ msec in the afterglow for small (top trace) and high (bottom trace, reduced gain) power levels. With increasing power level the spatial damping is reduced until the wave finally propagates undamped. Fig. 3b shows the wave intensity $|E^2|$ vs. radial ($\perp\underline{B}_o$) position at different axial ($||\underline{B}_o$, distances from the exciter at a small power level and Fig. 3c similarly at a high power level. At small amplitudes the radiation diverges from the dipole which accounts for most of the observed amplitude decay with distance. However, at high power levels the wave energy is confined to a narrow region of diameter $d \sim 5$ cm which does not broaden with increasing distance up to $20\lambda_{||} \approx 100$ cm along $\underline{B}_o$. Thus, the large amplitude wave has created a field aligned duct in which it is perfectly guided. The guided waves are plane waves as determined from phase measurements across the duct ($\phi_{(r)}=kz=\text{const}$). Once the duct has been created one can also guide small amplitude Whistler waves at other frequencies in it. After the end of the large amplitude Whistler wave pulse the duct decays within approximately 500 μsec. The build-up time depends on power level and is approximately 50 μsec at $P_{max} = 80$W.

Evidently, the duct is formed by changing some basic plasma parameters. We have therfore performed sampled Langmuir probe measurements in the duct region during and after the perturbing rf pulse. Fig. 4 shows Langmuir probe traces at

3 msec in the afterglow with and without the large amplitude Whistler waves. A plane thin Langmuir probe (4mm x 4mm x 0.2mm) is used which is once aligned with its surface normal parallel to $\underline{B}_o$ so as to measure $T_{e||}$ and then rotated by 90° so as to collect mainly electrons across $\underline{B}_o$ (electron Larmor radius $r_{ce} \approx 0.5$mm > probe thickness). In the absence of the Whistler wave $T_{e||} \approx T_{e\perp} \approx 0.28$eV but after a 1 msec rf burst (80W applied power) the electrons have been strongly heated ($T_{e||} \approx .79$eV, $T_{e\perp} \approx 1.06$eV), a temperature anisotropy has developed ($T_{e\perp}/T_{e||} \gtrsim 1.35$),^{5} $f_e(v_\perp)$ deviates from a Maxwellian due to an energetic tail and the electron density has decreased. These modifications occur only in the duct region. By sampling the probe characteristics after the end of the rf burst and observing the temperature relaxation we have verified that the results are not caused by rf rectification on the probe sheath.

The above described experimental observations may support the following qualitative physical picture of the nonlinear interaction: the wave electric field which is perpendicular to $\underline{B}_o$ and rotates in the same sense as the electrons increases $v_{e\perp}$. Energy conservation implies that between collisions ($t_{coll} \sim 1000 \times 2\pi/\omega$) $v_{e||}$ has to decrease which gives rise to the anisotropy. This process is particularly effective for resonant particles ($\omega - \omega_{ce} = k_{||}v_e$) which can form a tail on the distribution function. For longer time scales ($t \gg t_{coll}$) collisions limit the growth in anisotropy and the development of energetic tails and give rise to the observed heating. Temperature anisotropies and fast tails in $f_e(v_\perp)$ decrease the Whistler wave damping. Thus a positive feedback exists between the wave amplitude and its modification of the electron distribution function. At large applied signals the antenna radiation pattern is amplitude dependent. First, the electrons in the center region of the dipole pattern are perturbed. This leads to less damping, larger amplitudes, more perturbation etc. until the waves all propagate along a field aligned duct of anisotropic plasma which is on axis with the dipole and of comparable radial dimensions. During the collapse of the broad radiation pattern the amplitude in the duct increases in time as shown in Fig. 2b.

Due to the electron heating in the duct the particle diffusion is enhanced and the electron density decreases. The wavelength change in Fig. 2a ($\delta\lambda/\lambda \sim 5\%$) indicates a density drop of approximately $\delta n/n = 10\%$. Although this density perturbation contributes to the ducting process it is unlikely to explain the almost perfect guiding alone; for example, little ducting is seen in comparable density perturbations produced by probe shadows.

The observed self ducting of large amplitude Whistlers could be of great importance in space applications. Antenna reciprocity is violated, propagation oblique to $\underline{B}_o$ refracts along $\underline{B}_o$, resonance cone patterns vanish, etc.

The author gratefully acknowledges most fruitful discussions with R.W. Fredricks, F. Coroniti, D. Arnush, and the technical assistance by W. Dabbs and W. Daley.

REFERENCES

1. R.A. Helliwell, Whistlers and Related Ionospheric Phenomena, Stanford University Press, Stanford, Ca. (1965).
2. J.R. Wait, Electromagnetics and Plasmas, Holt, Rinehart and Winston. New York (1968); J.O. Thomas and B.J. Landmark, Plasma Waves in Space and in the Laboratory, Elsevier, New York, (1969, 1970).
3. R.F. Lutomirski and R.N. Sudan, Phys. Rev. 147, 156 (1966); P. Palmadesso and G. Schmidt, Phys. Fluids 15, 485 (1972); S.L. Ossakow, E. Ott and I. Haber, Phys. Fluids 15, 2314 (1972).
4. B.D. Fried and S.D. Conte, The Plasma Dispersion Function, Academic Press, New York (1961).
5. This measurement should only be considered as a qualitative indication for the anisotropy since probe measurements in B-fields can be subject to errors.

FIGURE CAPTIONS

Fig. 1. Normalized radial density profile with antenna size and location as indicated.

Fig. 2.(a) Typical time sequence of the pulsed plasma and sampled interferometer measurements.

(b) Interferometer signal vs. time at different rf power levels applied to the exciter dipole. Axial distance z_1 = 95 cm, ω/ω_c = 0.85.

Fig. 3.(a) Interferometer trace vs. axial position at small applied rf power levels (top trace) and large levels (bottom trace, reduced gain), sampled at afterglow time t_a.

(b) Radial wave intensity profiles at small power levels showing divergent radiation pattern.

(c) Wave intensity vs. r at different distances z from exciter antenna driven at large rf power levels. The wave has created a field aligned duct in which it propagates undamped. Afterglow time t_a = 3 msec.

Fig. 4. Sampled Langmuir probe traces at afterglow time t_a = 3 msec in the absence (top traces) and presence (bottom traces) of a large amplitude Whistler wave burst. Probe location r = 0, z = 50 cm.

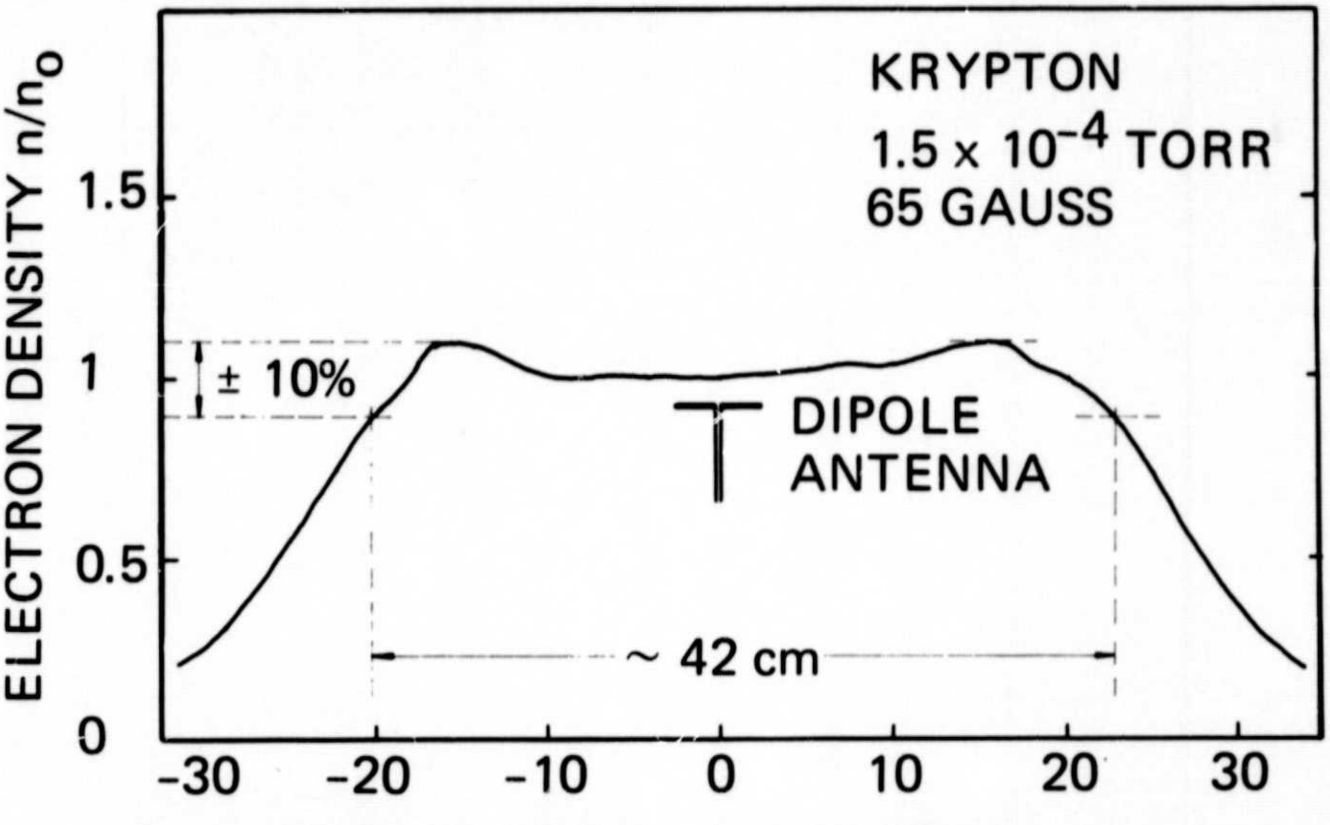
KRYPTON
1.5 x 10^{-4} TORR
65 GAUSS
± 10%
DIPOLE
ANTENNA
~ 42 cm
ELECTRON DENSITY n/n_o
1.5
1
0.5
0
-30
-20
-10
0
10
20
30
RADIAL POSITION ACROSS B_o r (cm)

Figure 1.

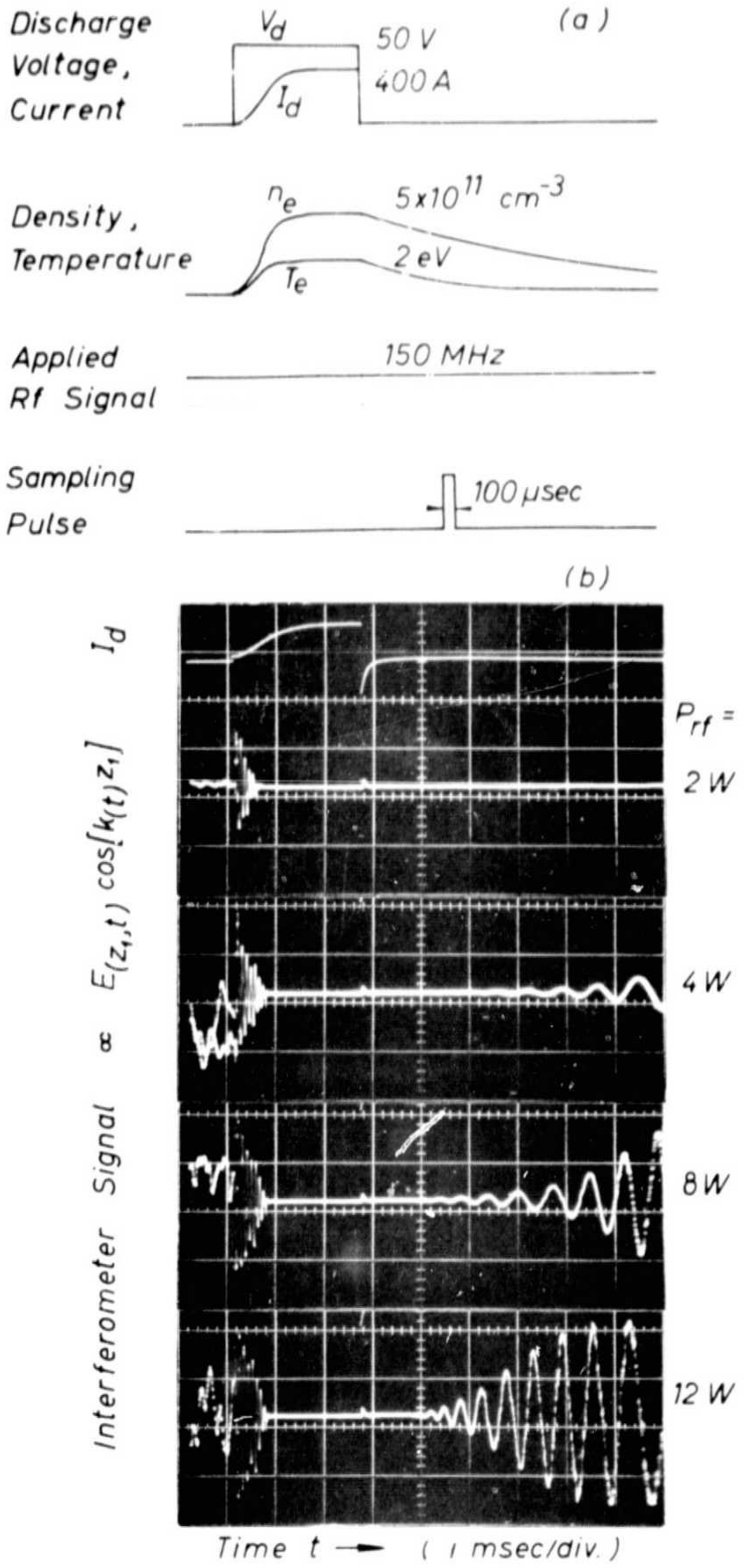
(a)
Discharge Voltage, Current
V_d
50 V
I_d
400 A
Density, Temperature
n_e
5×10^{11} cm^{-3}
T_e
2 eV
Applied Rf Signal
150 MHz
Sampling Pulse
100 μsec
(b)
I_d
P_{rf} =
2 W
4 W
8 W
12 W
Interferometer Signal $\propto$ $E_{(z_1,t)} \cos[k_{(t)} z_1]$
Time t → (1 msec/div.)

Figure 2.

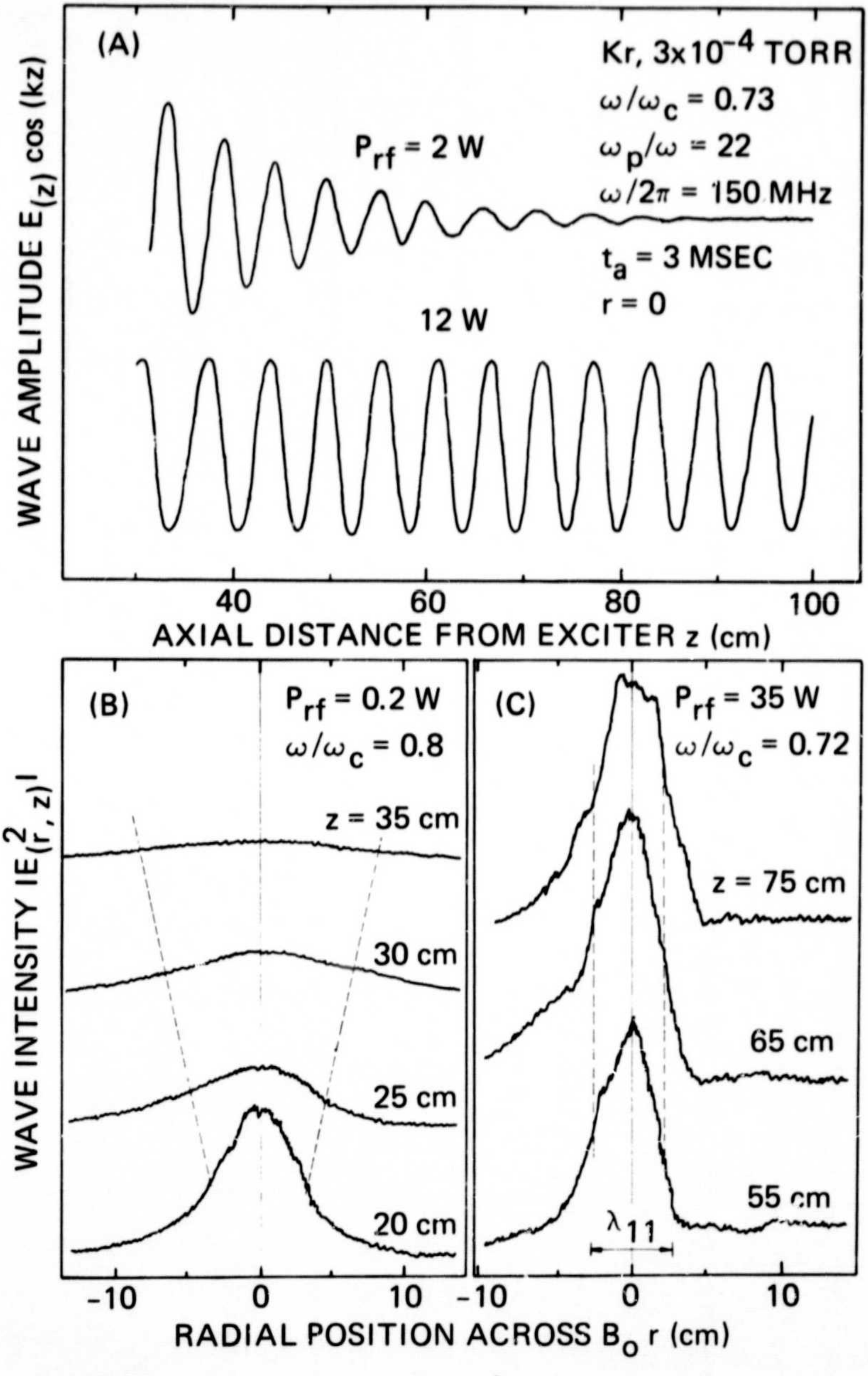
(A)
Kr, 3x10^{-4} TORR
$\omega/\omega_c = 0.73$
$\omega_p/\omega = 22$
$\omega/2\pi = 150$ MHz
$P_{rf} = 2$ W
$t_a = 3$ MSEC
$r = 0$
12 W
WAVE AMPLITUDE $E_{(z)} \cos(kz)$
40
60
80
100
AXIAL DISTANCE FROM EXCITER z (cm)
(B)
$P_{rf} = 0.2$ W
$\omega/\omega_c = 0.8$
z = 35 cm
30 cm
25 cm
20 cm
(C)
$P_{rf} = 35$ W
$\omega/\omega_c = 0.72$
z = 75 cm
65 cm
55 cm
λ_{11}
WAVE INTENSITY $|E^2_{(r,z)}|$
-10
0
10
-10
0
10
RADIAL POSITION ACROSS B_o r (cm)

Figure 3.

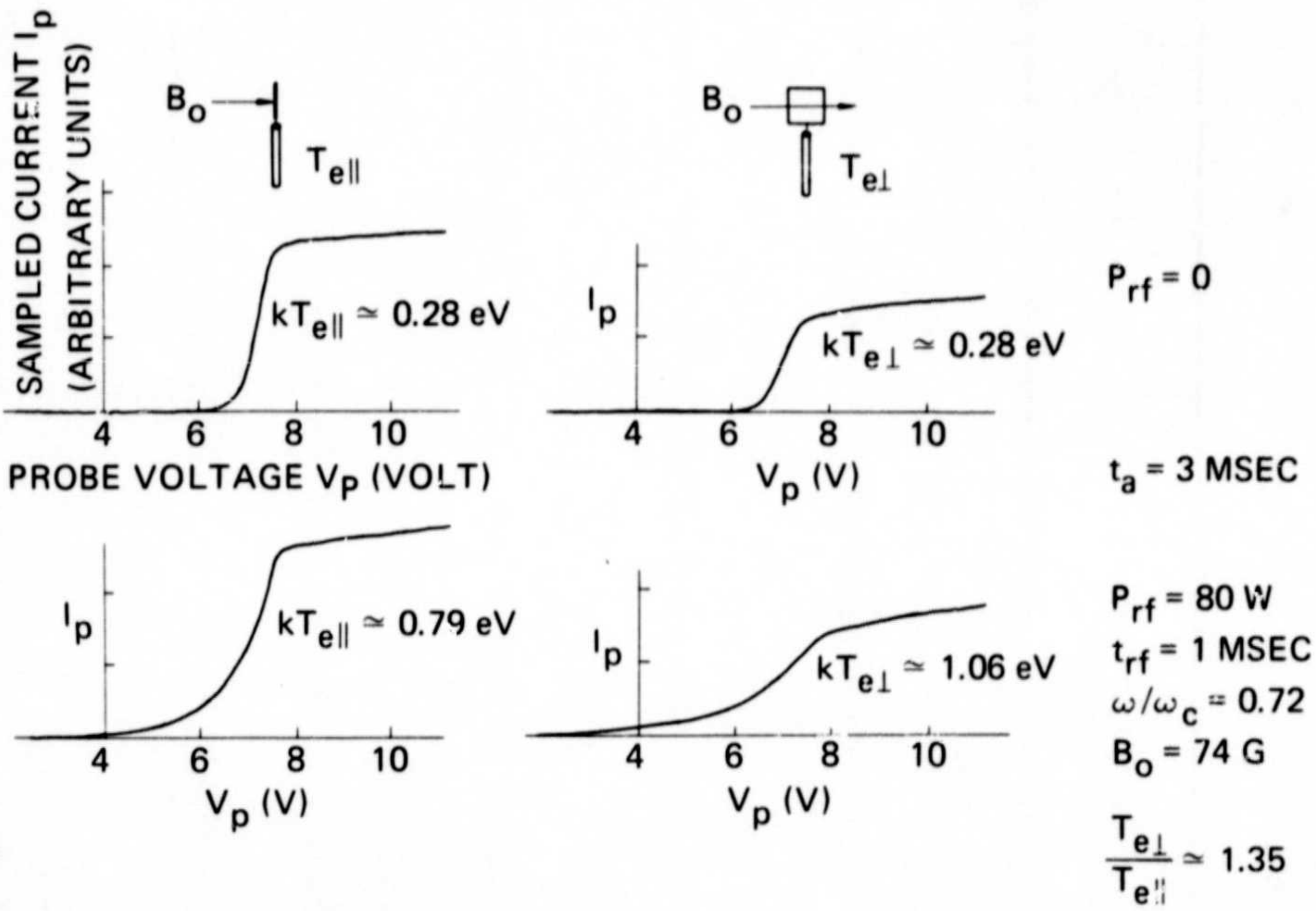
SAMPLED CURRENT I_p (ARBITRARY UNITS)
B_o
$T_{e\parallel}$
$kT_{e\parallel} \simeq 0.28$ eV
4
6
8
10
PROBE VOLTAGE V_p (VOLT)
B_o
$T_{e\perp}$
I_p
$kT_{e\perp} \simeq 0.28$ eV
4
6
8
10
V_p (V)
$P_{rf} = 0$
$t_a = 3$ MSEC
I_p
$kT_{e\parallel} \simeq 0.79$ eV
4
6
8
10
V_p (V)
I_p
$kT_{e\perp} \simeq 1.06$ eV
4
6
8
10
V_p (V)
$P_{rf} = 80$ W
$t_{rf} = 1$ MSEC
$\omega/\omega_c = 0.72$
$B_o = 74$ G
$\frac{T_{e\perp}}{T_{e\parallel}} \simeq 1.35$

Figure 4.